

# Reconfigurable topological lasing through Thouless pumping in bilayer photonic crystal

D.-H.-Minh Nguyen,<sup>1,2,\*</sup> Dung Xuan Nguyen,<sup>3,4,†</sup> H. Chau Nguyen,<sup>5</sup> Thibaud Louvet,<sup>6</sup> Emmanuel Drouard,<sup>6</sup> Xavier Letartre,<sup>6</sup> Dario Bercioux,<sup>1,7,‡</sup> and Hai Son Nguyen<sup>6,8,§</sup>

<sup>1</sup>*Donostia International Physics Center, 20018 Donostia-San Sebastián, Spain*

<sup>2</sup>*Advanced Polymers and Materials: Physics, Chemistry and Technology, Chemistry Faculty (UPV/EHU), Paseo M. Lardizabal 3, 20018 San Sebastián, Spain*

<sup>3</sup>*Brown Theoretical Physics Center and Department of Physics, Brown University, 182 Hope Street, Providence, Rhode Island 02912, USA*

<sup>4</sup>*Center for Theoretical Physics of Complex Systems, Institute for Basic Science (IBS), Daejeon, 34126, Republic of Korea*

<sup>5</sup>*Naturwissenschaftlich-Technische Fakultät, Universität Siegen, Walter-Flex-Straße 3, 57068 Siegen, Germany*

<sup>6</sup>*Ecole Centrale de Lyon, INSA Lyon, Université Claude Bernard Lyon 1, CPE Lyon, CNRS, INL, UMR5270, Ecully 69130, France*

<sup>7</sup>*IKERBASQUE, Basque Foundation for Science, Euskadi Plaza, 5, 48009 Bilbao, Spain*

<sup>8</sup>*IUF, Université de France*

(Dated: February 20, 2025)

We propose a programmable photonic platform that integrates Thouless pumping and reconfigurable lasing in sliding bilayer photonic crystals. By engineering two periodic potentials – a slowly moving photonic grating atop a stationary one – we demonstrate how their interplay yields distinct topological phases characterized by either robust light transport (Thouless pumping) or localized spatial oscillation (trapping). A heterojunction between crystals in these two regimes supports an interface mode stemming from the topological phase transition across the boundary. This interface mode can be actively tuned via microelectromechanical systems or switched through the integration of phase-change materials. We further establish the feasibility of lasing action at this interface mode, offering a pathway toward topologically robust and reconfigurable lasers. Our findings provide a framework for exploring topological phase transitions and unify the fields of topological photonics and programmable photonic devices, opening avenues for multidimensionally tunable light sources.

## I. INTRODUCTION

In 1981, Laughlin ingeniously explained Klitzing’s observation of the integer quantum Hall effect [1] with a picture of electrons being pumped from the inner edge of a Corbino disk to its outer perimeter [2]. This profound argument inspired Thouless, Kohmoto, Nightingale, and den Nijs to find the connection between the Hall conductance and the structure of the Landau levels [3], laying one of the foundation stones in topological research in physics. In 1983, Thouless proposed a simplified model of charge pumping similar to the quantum Hall effect [4], now known as Thouless pumping, which demonstrated quantized particle transport driven by a slowly varying potential. This model has become a cornerstone of topological transport phenomena since then and remains a subject of active research [5–14].

Here, we introduce a sliding bilayer photonic crystal platform to explore topological pumping in a novel framework: the competition between periodic potentials in their relative strengths. While Thouless’s seminal work addressed particle transport in a time-dependent poten-

tial composed of multiple periodic components, primarily focusing on the effects of competing periods, the impact of competing potential strengths has remained largely unexplored. Through comprehensive numerical simulations, supported by an effective analytical model, we demonstrate that tuning the relative strengths of these periodic potentials induces a topological phase transition, shifting the system from a pumping regime characterized by light transport to a trapping regime marked by spatial oscillation of light.

To investigate the consequences of this phase transition, we design a heterostructure configuration incorporating phase-change materials (PCMs). This configuration supports an interface mode at the boundary between the distinct topological phases, which arises from the phase transition across the heterojunction. The properties of this interface mode can be dynamically tuned using microelectromechanical systems or switched by inducing the crystal-to-amorphous transition in the PCM, enabling precise control over its behavior.

Furthermore, we demonstrate the feasibility of single-mode lasing at this topologically protected interface mode. This lasing action is highly reconfigurable, harnessing the chiral nature of the interface mode to achieve robust and tunable laser operation. Our numerical findings extend Thouless’s fundamental concept into a versatile photonic platform, providing a blueprint for designing novel photonic devices that exploit topological ro-

\* [d.h.minh.ng@gmail.com](mailto:d.h.minh.ng@gmail.com)

† [dungmuop@gmail.com](mailto:dungmuop@gmail.com)

‡ [dario.bercioux@dipc.org](mailto:dario.bercioux@dipc.org)

§ [hai-son.nguyen@ec-lyon.fr](mailto:hai-son.nguyen@ec-lyon.fr)

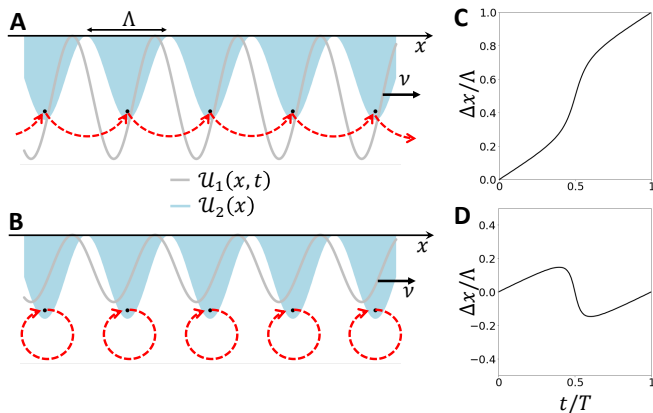


FIG. 1. **Revisiting Thouless pumping.** (A and B) Schematic drawings of two periodic potentials of the same periodicity where  $\mathcal{U}_1(x, t)$  moves slowly and  $\mathcal{U}_2(x)$  is stationary. The particles (denoted by black dots) can either be transported by  $\mathcal{U}_1(x, t)$  to the next unit cell (A), or be pulled back by  $\mathcal{U}_2(x)$  to their original positions (B). (C and D) Exemplary changes in position of a particle in each case during a pumping cycle with sine potentials  $\mathcal{U}_1(x, t) = 2.2 \sin(2\pi x/\Lambda - 2\pi\nu t/\Lambda)$  (C) [ $\mathcal{U}_1(x, t) = 1.2 \sin(2\pi x/\Lambda - 2\pi\nu t/\Lambda)$  (D)] and  $\mathcal{U}_2(x) = 1.5 \sin(2\pi x/\Lambda)$ .

bustness and tunability for advanced light manipulation and lasing applications.

## II. RESULTS

### A. A bird’s eye view of Thouless pumping

Thouless pumping can be illustrated by considering spinless particles in a one-dimensional (1D) space subject to a time- and space-dependent periodic potential  $\mathcal{U}(x, t) = \mathcal{U}(x + \Lambda, t) = \mathcal{U}(x, t + T)$ , where  $\Lambda$  and  $T$  are the periodicity in space and time, respectively. There are  $N_p$  particles in each minimum of the potential. For simplicity, we assume  $N_p = 1$  and that each particle is in its ground state inside a well. As this potential is adiabatically shifted along the  $x$ -axis, the wells carry the particles with them, resulting in a displacement  $\Lambda$  of the particles per time period  $T$ . Consequently, the integral of the current over a time period is an integer value, i.e., 1, giving rise to quantized transport. The adiabatic condition is met if the potential changes slowly enough that the particles remain in their ground state throughout the process.

In his seminal work [4], Thouless proposed an example of  $\mathcal{U}(x, t)$  as a superposition of two periodic potentials:  $\mathcal{U}(x, t) = \mathcal{U}_1(x, t) + \mathcal{U}_2(x)$ . Here,  $\mathcal{U}_1(x, t) = \mathcal{U}_1(x - \nu t)$  is a potential sliding slowly at a velocity  $\nu$  whereas  $\mathcal{U}_2(x)$  remains stationary. Both potentials share the same spatial period  $\Lambda$ , as depicted in Figs. 1A and 1B. We realize that the particles’ motion depends on the competition between the mobile  $\mathcal{U}_1(x, t)$  and the station-

ary  $\mathcal{U}_2(x)$ . While  $\mathcal{U}_1(x, t)$  tends to push the particles to induce pumping,  $\mathcal{U}_2(x)$  exerts a counteracting force and tends to localize them. When the driving potential  $\mathcal{U}_1(x, t)$  dominates, the particles are transported by a distance  $\Lambda$  at the end of a pumping cycle, as depicted in Figs. 1A and 1C. Conversely, if the stationary potential is stronger (Fig. 1B), the particles return to their original positions at  $t = T = \Lambda/\nu$  — see Fig. 1D. We term the latter regime “trapping” of particles. For a dynamic visualization of these scenarios, readers may refer to the Supplementary Materials (SMs) for animations of Figs. 1A and 1B.

### B. Bilayer photonic crystal

In photonic crystals, the absence of quantized charge prevents the observation of quantized transport as seen in the integer quantum Hall effect. However, in these systems, we can observe an analogy to the electron motion central to Thouless pumping by, for example, tracking the spatial variation of the input light beam [5, 7, 8]. Accordingly, we propose a realization of the bipartite potential described above in a 1D bilayer photonic crystal that comprises two parallel, high-contrast gratings separated by a distance  $d$ , as depicted in Fig. 2A. The two gratings share the same period  $\Lambda$  and are laterally displaced by  $\delta$ . They have thicknesses  $h_\ell$ , widths  $w_\ell$ , and refractive indices  $n_\ell$ , where  $\ell = 1, 2$ . All geometrical parameters are of subwavelength scale. As we shall see later, the upper and lower layers represent the potentials  $\mathcal{U}_1(x, t)$  and  $\mathcal{U}_2(x)$ , respectively.

In this work, we focus on the transverse electric (TE) modes, whose  $E_y$ -components can be described by four guided plane waves: two traveling right and two traveling left, within the upper and lower layers — see Fig. 2B. In each layer, diffraction causes counter-propagating modes travelling with velocities  $\pm v_\ell$  to couple at wave vector  $k_x = \pi/\Lambda$  (i.e., the  $X$  point of the first Brillouin zone) with a strength  $U_\ell$  that depends on the grating’s geometry and material. Plane waves traveling in the same direction but in different layers interact through their evanescent fields with strength  $V$ . This coupling amplitude can be adjusted by varying the interlayer separation  $d$ . The effective Hamiltonian describing the four lowest-frequency guided modes reads [15–17]

$$H(k, \delta) = \begin{pmatrix} \omega_1 + v_1 k & U_1 e^{-i2\pi\frac{\delta}{\Lambda}} & V & 0 \\ U_1 e^{i2\pi\frac{\delta}{\Lambda}} & \omega_1 - v_1 k & 0 & V \\ V & 0 & \omega_2 + v_2 k & U_2 \\ 0 & V & U_2 & \omega_2 - v_2 k \end{pmatrix}, \quad (1)$$

where  $k = k_x + \pi/\Lambda$  is the wave vector measured from the  $X$  point;  $\omega_1$  and  $\omega_2$  are the frequency offsets in the upper and lower gratings. The phase  $e^{\pm i2\pi\frac{\delta}{\Lambda}}$  in the intralayer coupling of the upper layer is induced by its displacement  $\delta$  — see the SM for a detailed derivation of the

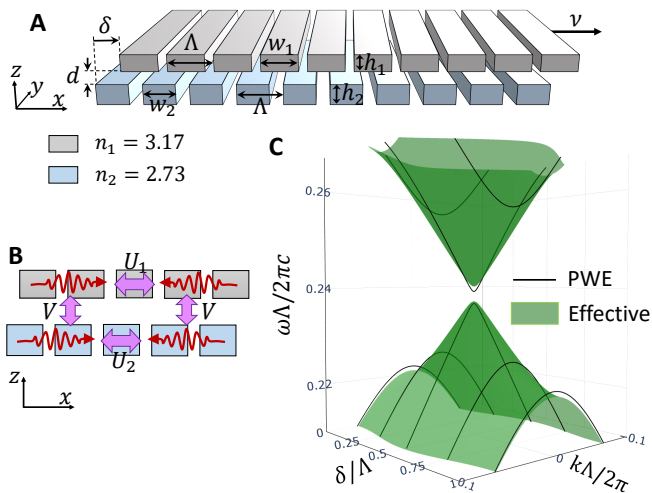


FIG. 2. **Bilayer photonic crystal.** (A) A bilayer photonic crystal composed of two gratings corrugated along the  $x$  direction with the same period  $\Lambda$ . The gratings are made of materials with refractive indices  $n_1$  and  $n_2$ . The upper layer slides slowly at velocity  $\nu$ , resulting in a lateral displacement  $\delta = \nu t$  relative to the lower layer at time  $t$ . (B) Sketch of guided plane waves (red arrows) and their intra- and interlayer coupling mechanisms. (C) Dispersion of the two lowest guided TE bands of config. (1) for various values of  $\delta$ . The green surfaces represent the effective model, while the black lines correspond to PWE simulations. Parameters:  $w_1 = 0.8\Lambda$ ,  $h_1 = 0.3\Lambda$ ,  $w_2 = 0.81\Lambda$ ,  $h_2 = 0.46\Lambda$ , and  $d = 0.1\Lambda$ .

effective Hamiltonian.

We are interested in the two lowest TE-guided modes. Using the concept of synthetic momentum (detailed in the Materials and Methods section), we find that the two cases  $U_1 > U_2$  and  $U_1 < U_2$  correspond to the pumping and trapping regimes in the bilayer photonic crystal, respectively. Although numerous designs of the bilayer crystal would yield similar results, we choose two exemplary configurations: config. (1) with  $(w_1, h_1, w_2, h_2) = (0.8, 0.3, 0.81, 0.46)\Lambda$ , and config. (2) with  $(w_1, h_1, w_2, h_2) = (0.8, 0.3, 0.77, 0.5)\Lambda$ . The former configuration has  $U_1 > U_2$ , and the latter has  $U_1 < U_2$ . The interlayer distance is fixed at  $d = 0.1\Lambda$ . In both cases, the upper and lower gratings are made of materials with refractive indices  $n_1 = 3.17$  and  $n_2 = 2.73$ , respectively. Potential materials for  $n_1$  are amorphous silicon (a-Si), indium phosphide (InP), and gallium arsenide (GaAs), while the refractive index  $n_2$  can be realized in titanium dioxide (TiO<sub>2</sub>), amorphous antimony trisulfide (Sb<sub>2</sub>S<sub>3</sub>) or aluminum arsenide (AlAs).

For the bilayer photonic crystal to experience all possible displacement configurations, we slowly translate the upper layer along the  $x$ -axis at a velocity  $\nu \ll v_\ell$  so that  $\delta = \nu t$  (Fig. 2A). The adiabatic condition is ensured since we choose the velocity to be sufficiently small so that the photonic modes at each instant are still accurately described by Hamiltonian (1), with negligible influence from the motion. Owing to the lattice translation sym-

metry, the system is invariant under the transformation  $\delta \rightarrow \delta + \Lambda$ . The black lines in Fig. 2C show the two lowest bands of config. (1) for several values of  $\delta$ , simulated using the plane wave expansion (PWE) method with the MIT Photonic Bands package [18]. By fitting the effective model’s dispersion to the PWE simulation results at  $\delta = 0$ , we retrieve all necessary parameters (see SM for details), and then plot the two lowest bands of Hamiltonian (1) in Fig. 2C (green surfaces), which shows good agreement between the effective model and PWE simulations. The two bands remain separated for all values of  $\delta$ . The lowest band reaches a maximum while the other minimizes at  $k = 0$  and  $\delta = 0.5\Lambda$ .

### C. Photonic pumping and trapping

We now show that the bilayer photonic crystal realizes the pumping and trapping regimes, with the mobile upper layer representing  $\mathcal{U}_1(x, t)$  and the stationary lower layer corresponding to  $\mathcal{U}_2(x)$ . However, since we cannot define any “particle” in such a photonic crystal, what is pumped or trapped here is the electromagnetic field localized in the dielectric rods of this crystal, i.e., energy. To track the motion of this localized field within a unit cell during a pumping cycle, we choose its center to be the Wannier center [19–21]. The change in position of the field’s center is given by

$$\Delta x_W(t) = -\frac{\Lambda}{2\pi} \int_0^t dt' \int_{-\pi/\Lambda}^{+\pi/\Lambda} dk \Omega(k, t'), \quad (2)$$

where  $\Omega(k, t') = i \left( \langle \frac{\partial u_1}{\partial k} | \frac{\partial u_1}{\partial t} \rangle - \langle \frac{\partial u_1}{\partial t} | \frac{\partial u_1}{\partial k} \rangle \right)$  is the Berry curvature, and  $|u_1\rangle$  represents the eigenstate of the lowest-frequency band. At the end of the pumping cycle,  $x_W$  changes by  $\Lambda$  if the localized field is successfully pumped, and remains unchanged (i.e.,  $\Delta x_W = 0$ ) if it is trapped.

The change in position of the Wannier center for both configurations (1) and (2) is efficiently computed using the effective model and visualized in Fig. 3. Indeed, we see that the Wannier center shifts to next unit cell in config. (1), signifying pumping (Fig. 3A), while it returns to its initial position at  $t = T$  in config. (2), indicating trapping (Fig. 3B). We look at the electric field distribution of the lowest mode obtained from PWE simulations to gain a deeper insight into how the fields vary. In both configurations, the electric field localizes in the dielectric rods of both layers across a wide range of wave number  $k$ , with the strongest localization at  $k = 0$  — see the insets of Figs. 3A and 3B. However, different behaviors emerge: In config. (1), the field follows the upper layer and gets dragged to the next unit cell, analogous to a particle pulled by the potential  $\mathcal{U}_1(x, t)$ . In config. (2), the localized field tends to stay in the initial unit cell with the lower layer, despite being constantly driven by the upper layer. The electric field’s behavior resembles that of a particle perturbed by  $\mathcal{U}_1(x, t)$  but constantly

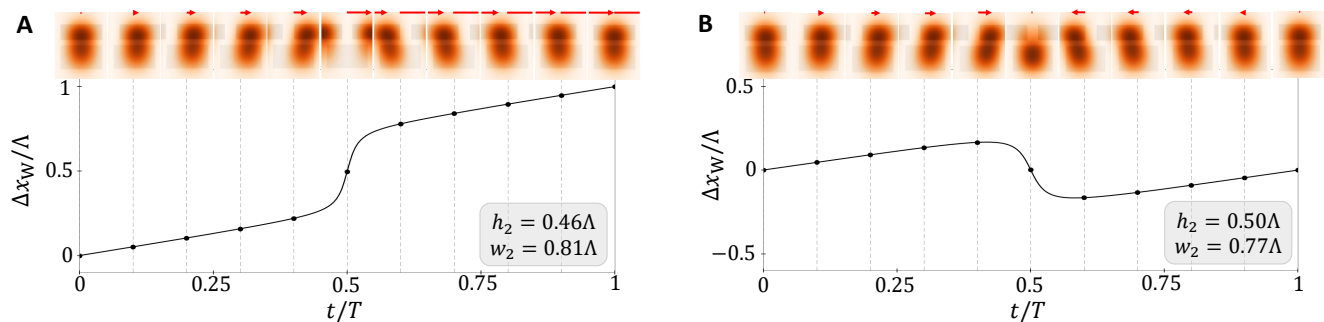


FIG. 3. **Pump versus trap.** (A and B) Pumping and trapping of localized electric field in bilayer photonic crystal. The position of the localized field is denoted by the variation of the Wannier center,  $\Delta x_W$ , within a unit cell during a pumping period  $T = \Lambda/\nu$ . If  $\Delta x_W$  changes by  $\Lambda$  (A) or remains unchanged (B) at the end of the period, the field’s center moves to the next unit cell or returns to its original position, respectively. The upper insets show the electric field distribution within a unit cell of the lowest mode at  $k = 0$  at various moments, obtained from PWE simulations. The red arrows indicate the corresponding displacement of the field. Here, the upper layer of the photonic crystal has  $h_1 = 0.3\Lambda$  and  $w_1 = 0.8\Lambda$  in both cases A and B, and the parameters of the lower layer are shown in the gray insets.

pulled back by  $\mathcal{U}_2(x)$ . Therefore, depending on the configuration, the bilayer photonic crystal can emulate either Thouless pumping or trapping of electromagnetic field — see SM for animations of the insets in Fig. 3.

#### D. Reconfigurable interface mode

In the context of Thouless pumping, by considering time ( $t$ ) as an additional dimension, the system can be examined in a  $(1+1)$ -D parameter space. Within this framework, the energy bands of the lattice are characterized by an invariant known as the Chern number [6, 20],  $C_n = -\Delta x_{Wn}(T)/\Lambda$  with  $n$  the band index, that identifies the topological phase of the system. In our case, the pumping and trapping regimes have different Chern numbers for the lowest band:  $C = -1$  and  $C = 0$ , respectively, indicating two distinct topological phases in the  $(1+1)$ -D space. By constructing a heterojunction of two photonic crystals with different topological phases, we expect to observe a robust interface mode protected by the topological phase transition across this heterojunction. This interface mode is pumped through the frequency gap as the lattice varies in time [20]. Hence, we consider a photonic heterojunction composed of config. (1) on the left (L) and config. (2) on the right (R), as illustrated in Fig. 4A. Since the upper layer of this heterojunction is a homogeneous grating, it can slide adiabatically at a velocity  $\nu$  without breaking the invariance of the system under the transformation  $\delta \rightarrow \delta + \Lambda$ .

The spectrum of this photonic heterojunction is obtained using the Finite-Difference Time-Domain (FDTD) method implemented in the solver 3D Electromagnetic Simulator of the commercial software Lumerical [22] — see Fig. 4B. As the upper layer slides to the right, a distinct mode, absent in the spectra of either config. (1) or (2) individually, traverses the spectral gap from one band to the other. In the vicinity of  $t = 0.5T$ , it sharply

contrasts with other modes for having a consistent descent in wavelength. Conversely, if the upper layer slides to the left, this mode’s wavelength monotonically increases. We refer to this behavior as “direction-locking” due to its dependence on the sliding direction of the upper layer. This phenomenon is known for the soliton mode in the Rice-Mele model [6, 20] and can be interpreted as a chiral edge mode along the synthetic dimension (see Materials and Methods). Indeed, by plotting the field distribution of this mode in Fig. 4D, we see that it strongly localizes at the interface of the heterojunction and exponentially decays into the constituent crystals with mismatched decay lengths. The decay lengths differ because the dispersions of the two crystals are different. This interface mode is robust against any perturbations that preserve the bulk spectral gap of both sides.

Since the interface mode acts as a cavity that confines electromagnetic field, we quantify this confinement by the mode’s quality (Q) factor. Figure 4E shows the Q-factor of the interface mode at various moments for two heterojunctions of different sizes. For the smaller heterojunction, this quantity varies greatly against time, or equivalently, the interlayer displacement  $\delta$ : it becomes smallest when the interface mode lies at the center of the spectral gap. This dependence wanes as the system size increases, and the Q-factor can attain values as high as  $10^5$ . This suggests potential applications of this photonic heterojunction in devices, such as lasers, beam emitter [23], and filters. A demonstration of this photonic heterojunction as a filter is provided in the SM.

*Dynamical transition of topological phases* — Motivated by a recent observation of topological phase transition in photonic crystal using phase-change material (PCM) [24], we demonstrate the dynamical control of topological interface mode in our bilayer lattice by incorporating a PCM into its design [25–31]. Specifically, the lower grating can be fabricated using amorphous anti-

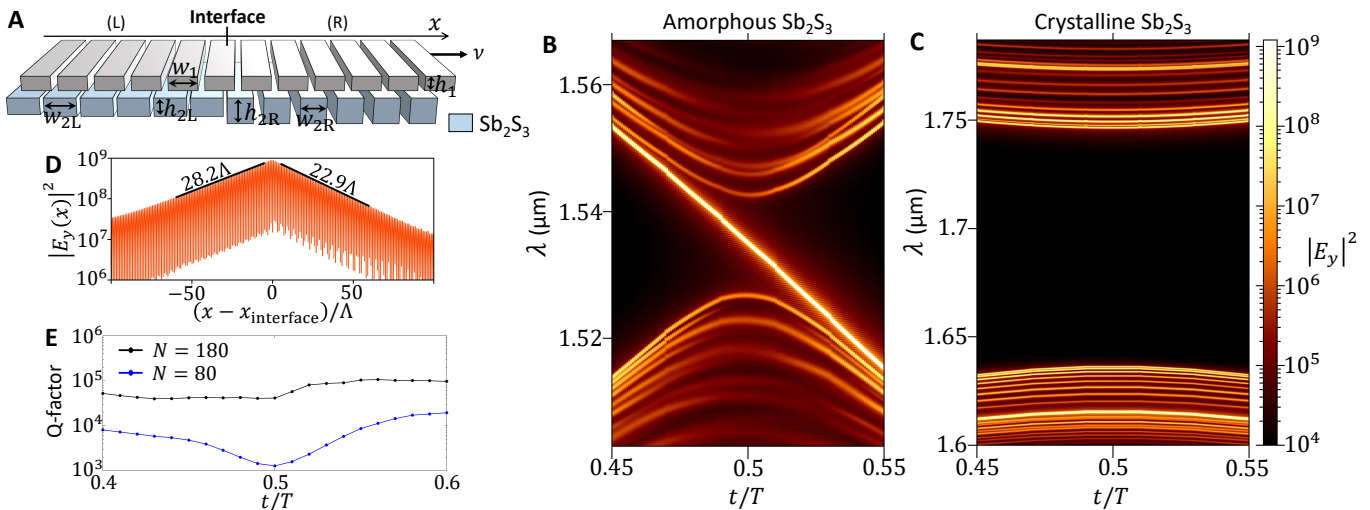


FIG. 4. **Heterojunction of bilayer photonic crystal.** (A) A photonic heterojunction in which the homogeneous upper grating slides with velocity  $\nu$  while the heterogeneous  $\text{Sb}_2\text{S}_3$  grating is stationary with heights and widths different on either side. The upper layer has  $w_1 = 0.8\Lambda$  and  $h_1 = 0.3\Lambda$ . The left (right) side of the  $\text{Sb}_2\text{S}_3$  layer has  $w_{2L(R)} = 0.81(0.77)\Lambda$  and  $h_{2L(R)} = 0.46(0.5)\Lambda$ . The interlayer distance is  $d = 0.1\Lambda$ . (B and C) The spectra of TE modes in the heterojunction when  $\text{Sb}_2\text{S}_3$  is in amorphous (B) and crystalline (C) phases, simulated by FDTD method. (D) The electric field profile  $|E_y(x)|^2$  of the interface mode in B at  $t = 0.5T$ , integrated over the  $z$  direction. (E) The quality factor of the interface mode in B with respect to time for two heterojunction sizes:  $N = 180$  and  $N = 80$ , where  $N$  is the number of periods on each side. The lattice period is  $\Lambda = 366$  nm.

mony trisulfide ( $\text{Sb}_2\text{S}_3$ ) [32–34], an earth-abundant and nontoxic PCM with ultralow losses.  $\text{Sb}_2\text{S}_3$  is stable at room temperature in both its amorphous ( $n_2 = 2.73$ ) and crystalline ( $n_2 = 3.26$ ) phases, which can be changed reversibly by either heating the entire sample or selectively illuminating it with laser pulses. The change in refractive index of the lower layer when  $\text{Sb}_2\text{S}_3$  transitions alters the coupling strengths between the guided waves. Thus, it may induce a topological phase transition in the bilayer photonic crystal, switching it between the pumping and trapping regimes (see Materials and Methods for a complete topological phase diagram). This phenomenon indeed occurs in our current photonic heterojunction where, upon the crystallization of  $\text{Sb}_2\text{S}_3$ , the photonic crystal on the left side of the heterojunction changes from the pumping to trapping regime while the right side remains in the trapping regime. The spectrum of the lowest spectral gap in the vicinity of  $t = 0.5T$  is shown in Fig. 4C when  $\text{Sb}_2\text{S}_3$  crystallizes completely. The gap widens and shifts to longer wavelength compared to Fig. 4B since the refractive index of the lower grating increases. Importantly, the interface mode traversing the gap disappears as the two sides of the heterojunction now share the same topology, which serves as a clear signature of the topological phase transition. This also illustrates how PCMs can be used to dynamically switch on and off an optical interface mode.

### E. Topological lasing

Owing to the high Q-factor and strong confinement of our photonic heterojunction, we can incorporate active (i.e., gain) materials into one layer and perform non-resonant optical excitation to induce lasing at the interface mode [35–39]. The lasing wavelength can be selectively and continuously varied through the dynamical sliding motion of the upper layer. In particular, we use the design of a photonic junction presented before (Fig. 4A) with the upper grating composed of InP and InAsP quantum wells (QWs). This layer is continuously illuminated by a non-resonant optical source of wavelength  $\lambda_e = 850$  nm (Fig. 5A). As sketched in Fig. 5B, the pump injects hot carriers to the conduction and valence bands of InP. These hot electrons and holes then relax to the fundamental states of the QWs and then recombine radiatively, leading to a spontaneous emission centered at wavelength  $\lambda_s = 1500$  nm. In the spontaneous emission, only photons of wavelength  $\lambda_L$  associated with the interface mode are in resonance and confined within the cavity; those of other wavelengths decay rapidly. After the electronic population inversion is established, lasing emission can be achieved precisely at the wavelength  $\lambda_L$ .

We numerically validate this idea through Lumerical FDTD simulations with the gain material modeled by a four-level two-electron material [40]. First, we examine the lasing action with the two layers displaced by  $\delta = 0.5\Lambda$ . By increasing the field strength of the pump, we observe an emission peak at  $\lambda_L$  for  $E_{\text{pump}} \gtrsim 7 \times 10^5$  V/m. The dependence of the lasing modal intensity on the

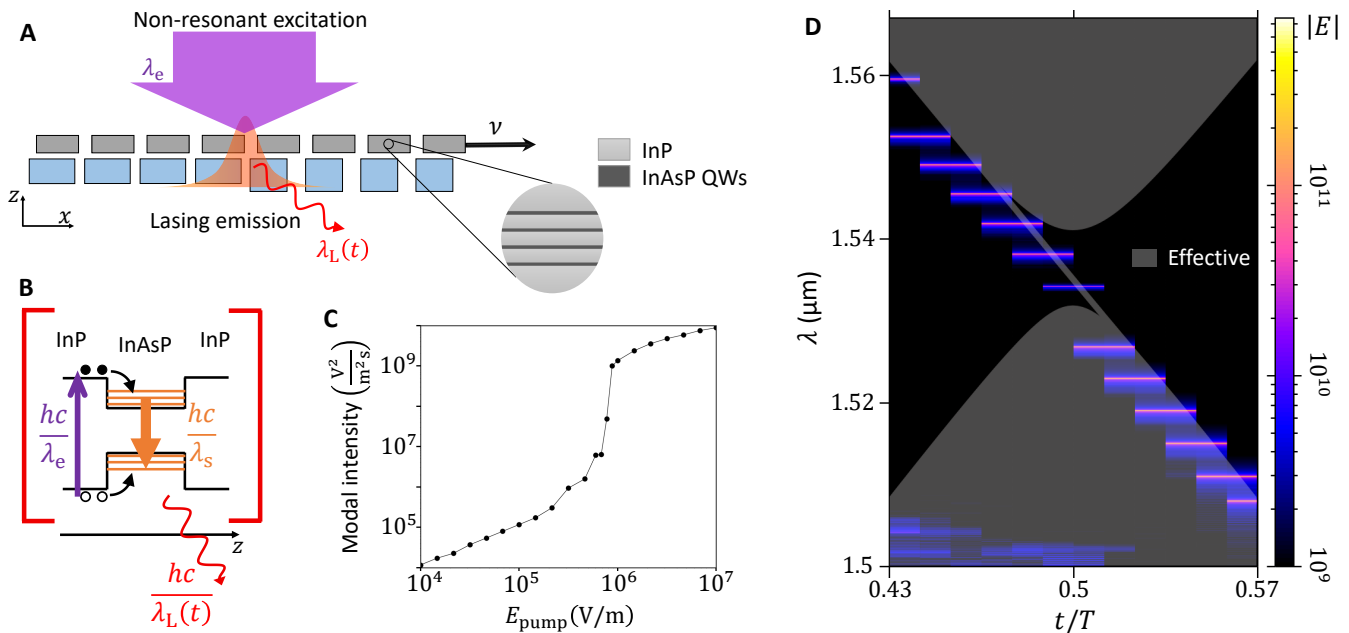


FIG. 5. **Direction-locking variation of lasing mode.** (A) The heterojunction of bilayer photonic crystal where the upper layer is made of gain material InAsP/InP moves slowly with velocity  $\nu$ . The heterojunction is continuously pumped by a non-resonant source of wavelength  $\lambda_e = 850$  nm and achieves lasing action at  $\lambda_L$ . (B) Schematic diagram of the four-level model for the lasing action with the spontaneous emission wavelength  $\lambda_s = 1500$  nm. (C) Dependence of modal intensity of the lasing signal at  $\delta = 0.5\lambda$  on the pump electric field strength. (D) Spectrum of the lasing mode at several moments  $t$  when the upper layer slides and the non-resonant source has an electric field strength  $1.3 \times 10^6$  V m $^{-1}$ . The gray line and areas indicate the interface and bulk modes following the effective model.

pump field strength is shown in Fig. 5C with the characteristic laser threshold behavior — a clear transition from spontaneous to stimulated emission. Here, the modal intensity is defined by  $\frac{1}{2\pi} \int d\omega |E|^2$  with the integration taken over the frequency range  $\omega$  encompassing the lasing peak.

Finally, translating the upper layer slowly at a fixed pump intensity yields the emission spectrum at various moments  $t$  shown in Fig. 5D, where the lasing peaks align with the interface mode. The variation of the lasing wavelength with respect to time is locked to the sliding direction of the upper layer. The spectrum obtained from the effective model is presented as a visual reference showing the interface mode's variation; it matches perfectly with the FDTD simulation of Fig. 4B. The presence of spontaneous emission in the spectrum at  $t \lesssim 0.5T$  means that the lasing threshold varies with respect to the relative displacement  $\delta$ . Single-mode lasing across a range of wavelengths can be achieved by constantly keeping the pump power above the threshold. This demonstrates the tunability of the lasing mode in this photonic heterojunction. Such a lasing mode is robust against defects and disorders since they are topologically protected. The single-mode operation is guaranteed as the number of edge mode is one, which is dictated by the change of Chern number across the heterojunction.

### III. DISCUSSION

In this work, we have revised the problem of particles moving in a time-dependent potential proposed by Thouless [4], which is a combination of two periodic potentials,  $\mathcal{U}(x, t) = \mathcal{U}_1(x - \nu t) + \mathcal{U}_2(x)$ . The competition between the mobile  $\mathcal{U}_1(x - \nu t)$  and the stationary  $\mathcal{U}_2(x)$  gives rise to two distinct regimes: pumping and trapping of particles. We have shown that these two regimes can be observed in two configurations of a bilayer photonic crystal, in which the electromagnetic field localized within each unit cell is either pumped or trapped as the upper layer of this crystal slides slowly and unidirectionally. A photonic heterojunction composed of those two configurations has a localized interface mode that is pumped in frequency across the spectral gap during a pumping cycle. This interface mode has high Q-factor for a wide range of interlayer displacement  $\delta$ , and thus we further demonstrate that the heterojunction can be used as a cavity to achieve single-mode lasing. The lasing wavelength only decreases when the upper layer slides to the right and vice versa. Additionally, we have also revealed the possibility to switch the interface mode on and off using PCMs, which can serve as a signature of the topological phase transition.

Regarding the experimental feasibility, the bilayer photonic crystal can be fabricated using standard nanofabrication methods, such as electron beam lithography and

ionic dry etching [17, 41]. Dynamic control over the vertical and lateral degrees of freedom can be facilitated by microelectromechanical systems (MEMSs) [42–45]. Especially, a recent MEMS integrated into a bilayer photonic lattice has demonstrated its capability to dynamically tune various degrees of freedom, including the interlayer spacing, relative rotation, lateral translation, tilting, and stretching [46]. The phase of the PCM  $\text{Sb}_2\text{S}_3$  can be reversibly switched using state of the art microheaters [47], such as indium-tin-oxide heater [33, 48], silicon PIN diode heater [49, 50], or graphene-based heater [51].

Our proposal of combining MEMS and PCMs for dynamically controlling topological interface modes demonstrates the potential of this bilayer photonic heterojunction for realizing multidimensionally reconfigurable photonic devices. As applications, this includes lasers, beam emitters and filters, providing unprecedented mechanisms of creating and manipulating light. Fundamentally, our results also lay the groundwork for further investigations into 2D Thouless pumping, which is connected to the 4D quantum Hall effect [52, 53], and for examining Thouless pumping in moiré lattices, as predicted in twisted bilayer graphene [54, 55] and noted by Thouless himself [4]. Furthermore, this study opens avenues for exploring novel aspects of Thouless pumping beyond the adiabatic regime [56, 57] and even in the relativistic regime, where the grating motion approaches the speed of light [58, 59].

## IV. MATERIALS AND METHODS

### Topology in synthetic momentum space

Here, we present a study of the photonic spectra in the bilayer photonic crystal using the concept of synthetic momentum [60–64]. This method guides us to finding the Thouless pumping and trapping regimes in this system, and can be extended to investigate other novel phenomena. Hereafter, we use the terms ‘momentum’ and ‘wavevector’ interchangeably, as well as ‘energy’ and ‘frequency’.

Owing to the discrete translation symmetry of the lattice, i.e.,  $H(k, \delta + \Lambda) = H(k, \delta)$ , we define the interlayer displacement as a synthetic momentum [65, 66]

$$q = 2\pi \frac{\delta}{\Lambda^2}.$$

We, henceforth, consider the system’s frequency bands in a 2D synthetic momentum space  $(k, q)$ . Since  $q$  is even under time reversal, such a definition of the synthetic momentum permits the observation of nontrivial topological phases in this lattice equivalent to a system without time-reversal symmetry.

To understand the spectral properties of the system, we look at the simplest situation where  $\omega_1 = \omega_2 = \omega_0$  and

$v_1 = v_2 = v$ . The band structure obtained from Hamiltonian (1) is shown in Fig. 6A for nine cases, where the values of  $\Delta$  and  $\Gamma$  are  $\Delta = 0, \pm 0.05U$  and  $\Gamma = 0, \pm 0.1U$ . We choose  $U\Lambda = 0.02v$  in this figure and also express the momenta in units of  $2\pi/\Lambda$  hereafter. The four frequency bands may either overlap or be separated, depending on the parameters  $\Delta$  and  $\Gamma$  defined by

$$\Delta = \frac{U_1 - U_2}{2}, \quad \Gamma = U - \sqrt{V^2 + \Delta^2}.$$

We term the three regions between these bands the lower, middle, and upper gaps hereafter. When  $\Delta = 0$ , the upper and lower gaps close at a high symmetry point  $(k, q) = (0, 1/2)$ , forming a single Dirac point with linear dispersion along both  $k$  and  $q$  — see cases (II), (V), and (VIII) of Fig. 6A. We note that the range of  $q$  displayed in Fig. 6A extends beyond the first Brillouin zone to visualize the Dirac cone/gap at the zone boundary. As soon as  $\Delta \neq 0$ , this degeneracy point vanishes, creating a spectral gap. Meanwhile, the middle gap always closes for  $\Gamma = 0$  and forms a semi-Dirac point that disperses linearly along  $q$  and quadratically along  $k$  [67, 68], as shown in cases (IV)–(VI). For  $\Delta = 0$  and  $\Gamma < 0$ , the two middle bands touch at two Dirac points located at  $q = 0$  (VIII). Increasing  $\Gamma$  causes these points to approach each other and eventually merge into a single semi-Dirac point when  $\Gamma = 0$ . The middle gap opens once  $\Gamma > 0$  (II). This merging of Dirac points follows a generic mechanism proposed in Ref. [67, 68] for two Dirac points of opposite winding numbers. For  $\Delta \neq 0$  and  $\Gamma < 0$ , the middle gap opens and has two valleys related to the two aforementioned Dirac points. As  $\Gamma$  increases, these two valleys move toward each other and merge into a single valley. Once  $\Gamma = 0$ , the middle gap closes at a semi-Dirac point [cases (IV) and (VI)]. The gap opens again when  $\Gamma$  is positive.

To classify the topology of the spectral gaps, we use the Chern number, which is proportional to the flux of Berry curvature threading through the synthetic momentum space of all the bands below the gap. The Berry curvature of a band  $n$  in the synthetic momentum space  $(k, q)$  is computed from the effective Hamiltonian (1) using a gauge-invariant formula [69]

$$\Omega_n(k, q) = -2\Im \sum_{n' \neq n} \frac{\langle \psi_n | \partial H / \partial k | \psi_{n'} \rangle \langle \psi_{n'} | \partial H / \partial q | \psi_n \rangle}{(\omega_n - \omega_{n'})^2}$$

with  $\psi_n$  and  $\omega_n$  being the eigenvectors and eigenvalues of the effective Hamiltonian, respectively. The Chern number of each band is obtained by integrating its Berry curvature over the synthetic momentum space  $(k, q)$ ,

$$C_n = \frac{1}{2\pi} \int_{-\pi/\Lambda}^{+\pi/\Lambda} dq \int_{-K_c}^{+K_c} dk \Omega_n(k, q)$$

where  $K_c$  is a cutoff value of  $k$ . In Fig. 6A, we choose  $K_c = 0.5(2\pi/\Lambda)$ . We recall that Berry curvature emanating from the singularity (i.e., the band touching point) in a parameter space is similar to the magnetic field stemming from a magnetic monopole [20, 69]. Thus, if the

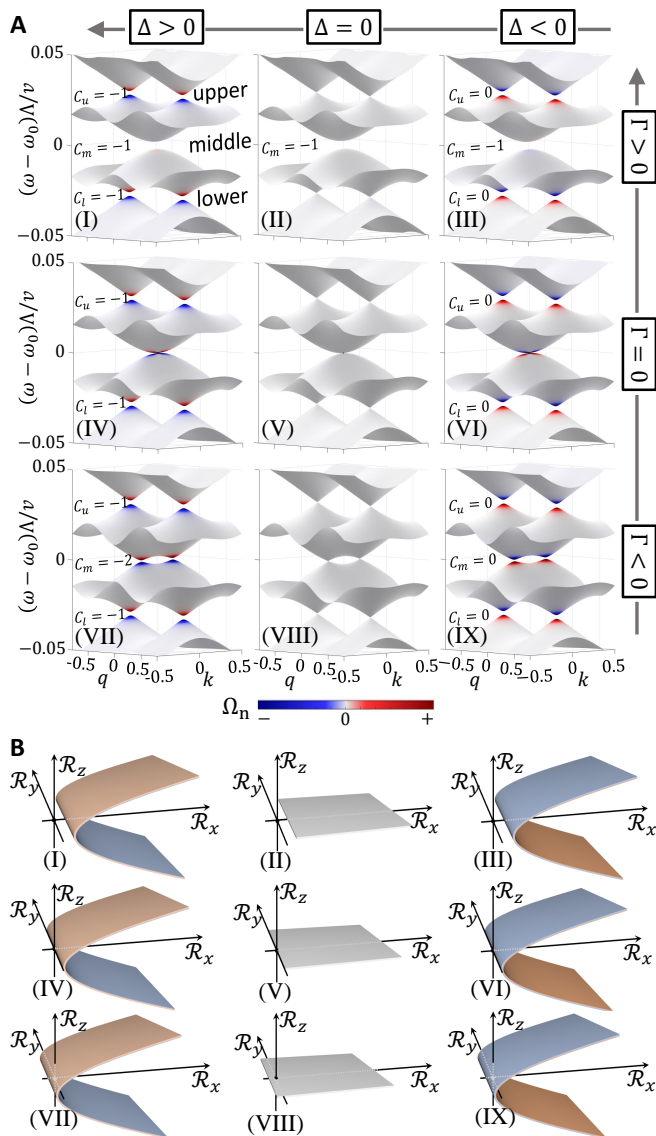


FIG. 6. **Topology in synthetic momentum space.** (A) Band structures and the associated local Berry curvature of the effective Hamiltonian for different values of  $\Delta$  and  $\Gamma$ . The Chern number of each spectral gap is proportional to the sum of the Berry flux of all bands below it. (B) The mappings of the momentum space onto the parameter space  $(\mathcal{R}_x, \mathcal{R}_y, \mathcal{R}_z)$  through the middle gap’s two-band model for each case (I-IX).

momentum space is a closed manifold, the Chern number is quantized and equal to the charge of the singularity. Here, the synthetic momentum space of Hamiltonian (1) is a semi-compact manifold that is closed along the synthetic momentum  $q$  but open and infinite along the genuine momentum  $k$ . Although Chern numbers are not well-defined on noncompact manifolds, the effective Hamiltonian (1) provides an efficient means to study the change in Chern numbers, similar to the Dirac Hamiltonian, which would lead to the emergence of chiral edge modes. Thus, the Berry curvature  $\Omega_n$  and Chern num-

bers are shown in Fig. 6A, depicting the topological phase transitions of the spectrum. For instance, across the transition from  $\Delta < 0$  to  $\Delta > 0$ , i.e., along the rows of Fig. 6A, the Chern numbers of the lower and upper gaps change by one unit, whereas that of the middle gap changes by two when  $\Gamma < 0$ .

To illustrate these topological transitions, we focus on an effective two-band Hamiltonian for each gap  $H_\alpha(k, q) = \omega_\alpha + \mathcal{R}_\alpha(k, q) \cdot \sigma$ . Here,  $\alpha$  is notated as “lower”, “middle”, or “upper”, and  $\sigma = (\sigma_x, \sigma_y, \sigma_z)$  is a vector of Pauli matrices. These two-band models are obtained from Hamiltonian (1) using the Löwdin partition method [70, 71] — see SM for detailed derivations. They are valid for a small range of  $q$  and thus reside on a noncompact manifold, which breaks the quantization of Chern numbers, e.g., the Chern numbers may become half-integer. Despite the change of Chern numbers due to the change of manifold topology, the difference between the Chern numbers in different phases stays the same. The lower and upper gaps have different frequency offsets  $\omega_\alpha$  but share the same  $\mathcal{R}$ -vector:

$$\mathcal{R}_{\text{lower/upper}}(k, \tilde{q}) = - \left( \tilde{r}vk, \tilde{r} \frac{U + \Delta}{2} \tilde{q}, \Delta \right)$$

with  $\tilde{q} = q - \pi/\Lambda$  and  $\tilde{r} = V/\sqrt{V^2 + U^2}$ . This is a Dirac Hamiltonian of mass  $\Delta$  and has been studied extensively in the literature [20, 69]. For nonzero Dirac mass, the gap has a Chern number of either  $+1/2$  [(III), (VI), (IX)] or  $-1/2$  [(I), (IV), (VII)]. Meanwhile, the middle gap is described by

$$\mathcal{R}_{\text{middle}}(k, q) \approx \left( \Gamma + \frac{U+2\Delta}{8}q^2 + \frac{3v^2k^2}{8U^2}, \frac{(U+\Delta)(V-\Delta)}{2V}q\Lambda, -\frac{\Delta}{V}vk \right)$$

with the condition  $\Delta \ll U, V$ . Using the mapping  $(k, q) \mapsto \mathcal{R}(k, q)$ , we map the momentum space onto an infinite 2D curved surface in the parameter space  $(\mathcal{R}_x, \mathcal{R}_y, \mathcal{R}_z)$  with the relation  $\mathcal{R}_x \approx \Gamma + \frac{3V^2}{8U\Delta^2}\mathcal{R}_z^2$ . Here, we have neglected the dependence of  $\mathcal{R}_x$  on  $\mathcal{R}_y$  since its coefficient is much smaller than that of  $\mathcal{R}_z$ . This image of the momentum space is a directed 2D surface: its two sides can be colored differently [20] — Fig. 6B. If the surface is wrapped around the singularity at the origin, it captures all the Berry flux from that point, and thus the Chern number is 1, as shown in case (IX) of Fig. 6B. If the surface is turned inside out and still wrapped around the singularity, the Chern number reverses its sign to be  $-1$  (VII). If the singularity lies outside the region enclosed by the surface, the total Berry flux threading through it is zero [(I)-(III)]. The surface becomes a semi-infinite plane  $h_z = 0$  whenever  $\Delta = 0$ . In all cases, if the surface passes through the singularity, the two middle bands become gapless.

It is noteworthy that in cases (III) and (IX) of Fig. 6A, the Chern number of the lower gap is zero despite the non-vanishing Berry curvature. This phenomenon arises from the contrasting behavior of the Berry curvature near and away from the band edge. While the Berry curvature is visibly strong and positive near the band edge, it

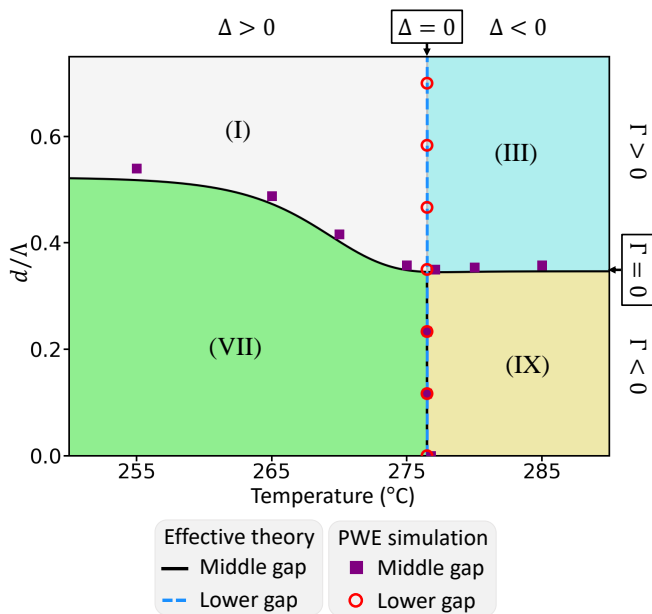


FIG. 7. **Phase diagram controlled by varying the temperature and interlayer distance.** The bilayer comprises an antimony trisulfide grating and an amorphous silicon grating. The solid black (dashed blue) line denotes where the middle (lower) gap closes within the effective theory. The purple squares (red circles) correspond to similar points obtained through PWE simulations.

becomes weak and negative in regions further away. The cancellation of these opposing contributions results in a net Chern number of zero.

Knowing the Chern numbers of the spectral gaps, we can identify the pumping ( $C \neq 0$ ) and trapping ( $C = 0$ ) regimes. For instance, the pumping and trapping regimes considered in the Results section correspond to cases (VII) and (IX), respectively. The parameters used for the effective model in Fig. 2C are  $\omega_1 = 0.27815(2\pi c/\Lambda)$ ,  $U_1 = 0.02232(2\pi c/\Lambda)$ ,  $v_1 = 0.37602c$ ,  $\omega_2 = 0.28010(2\pi c/\Lambda)$ ,  $U_2 = 0.02142(2\pi c/\Lambda)$ , and  $v_2 = 0.40454c$ . We can also design different types of heterojunction to observe different topological chiral modes, as presented in the SM.

#### Dynamic control of topological phases via phase-change material

The topological phases presented previously can be observed in a single sample by means of PCMs [24–31]. In this work, we incorporate into the bilayer photonic crystal the PCM antimony trisulfide ( $\text{Sb}_2\text{S}_3$ ), which is well known for its ultralow losses across the visible and near-infrared wavelengths in both crystalline and amorphous phases [72–74], and its exceptional tunability [33, 75, 76]. Its phase can be changed reversibly, either by heating the entire sample or by shining laser pulses at a specific spot. Besides,  $\text{Sb}_2\text{S}_3$  has been used in fabricating gratings [32]

and metasurfaces [33, 34].

In our bilayer system, as the intralayer coupling strength depends on the refractive index, we vary  $\Delta$  by switching the material’s phase between amorphous and crystalline. We demonstrate this idea by designing a bilayer system of an amorphous silicon (refractive index 3.15) grating and an  $\text{Sb}_2\text{S}_3$  grating. The geometrical parameters are  $w_1 = w_2 = 0.8\Lambda$  and  $h_1 = h_2 = 0.37\Lambda$ . The refractive index of  $\text{Sb}_2\text{S}_3$  increases continuously from 2.73 to 3.26 when it transitions from amorphous to crystalline phase. This transition is complete when the temperature is raised above  $280^\circ\text{C}$  [77]. Amorphization can be achieved by heating the crystalline  $\text{Sb}_2\text{S}_3$  above its melting temperature and then rapidly quenching. An on-chip reversible transition of PCM can be obtained using a state of the art microheater [33, 47–51, 78]. Here, by fitting the experimental data describing the temperature-dependent refractive index of  $\text{Sb}_2\text{S}_3$  during its crystallization [77], we obtained a function analogous to the logistic function

$$n_{\text{Sb}_2\text{S}_3} = A + B \left\{ 1 - \frac{1}{1 + 0.5 [e^{\alpha(T-T_0)} + e^{\beta(T-T_0)}]} \right\}$$

with  $A = 2.732738$ ,  $B = 0.530212$ ,  $\alpha = 0.47062 \text{ K}^{-1}$ ,  $\beta = 0.23360 \text{ K}^{-1}$ , and  $T_0 = 273 \text{ K}$ . The PWE simulations are run accordingly using this function. The dependence of parameters  $\omega_2$ ,  $v_2$ , and  $U_2$  of the PCM grating and the interlayer coupling  $V$  on temperature is achieved by fitting the effective model of the monolayer and bilayer lattices with PWE results. The experimental data of  $\text{Sb}_2\text{S}_3$  and the temperature dependence of the effective model’s parameters are presented in the SM.

On the other hand, to alter  $\Gamma$ , the interlayer distance can be adjusted dynamically using on-chip MEMSs [46, 79]. Such a combination of thermal and mechanical control of the bilayer grating allows us to achieve the complete phase diagram shown in Fig. 7 on a single sample, corresponding to  $\text{Sb}_2\text{S}_3$  crystallization. The four regions are associated with the four gapped states in Fig. 6A while their borders correspond to the gapless ones. These gap-closing lines match well with the results obtained from the PWE simulation using MIT Photonic Bands package [18].

The phase diagram is general and can be achieved with other dielectric materials as long as the geometrical parameters are appropriate. As considered above, despite replacing amorphous silicon with indium phosphide (InP), whose refractive index is 3.17, all the topological phases remain. This generality implies possible optimization of the bilayer grating for specific properties, such as the spectral gap or the quality factor of the heterostructure.

#### FDTD simulations

All the FDTD simulations in this work are carried out by either the MEEP package [80] or the commercial soft-

ware Lumerical [22].

**Spectrum** – The spectra shown in Figs. 4B and 4C of the photonic heterojunction are obtained from Lumerical FDTD simulations. A dielectric photonic junction is constructed following the geometry depicted in Fig. 4A with its interface lying at the center of the computational cell. The refractive indices of the upper and lower gratings are 3.17 and 2.73, respectively. In this linear regime, the parameters scale with the lattice constant  $\Lambda$ , so we set  $\Lambda = 1\ \mu\text{m}$  for simplicity. The total number of periods is 400, i.e., the length of the heterojunction is  $400\ \mu\text{m}$ . The 2D computational cell is enclosed in standard phase-matching layers. The mesh for finite-difference calculation has the maximum mesh step  $0.02\ \mu\text{m}$  along the  $x$  direction and 67 mesh cells per wavelength along the  $y$  direction (i.e.,  $z$  direction in Results). The electromagnetic modes of the system are excited by 20 electric dipoles randomly distributed in the bilayer within a range of  $160\ \mu\text{m}$  around the interface. The dipoles are aligned along the  $z$  axis ( $\theta = 0$ ), have random phases and random angle with respect to the  $x$  axis. Each of them emits a broadband pulse with frequency ranging from 69 THz to 74 THz. The simulation runs for 70 ps at 300 K. All signals are recorded and analyzed by 20 time monitors randomly distributed in the system within a range of  $240\ \mu\text{m}$  around the interface. We note that the spectra in Fig. 4 have a few discrete patterns. They are numerical artifacts resulting from the dielectric gratings crossing a mesh line.

**Quality factor** – The quality factor of the edge mode is computed using MEEP and Lumerical simulations, with both methods yielding comparable results. In the MEEP simulations, a dielectric photonic junction is constructed similar to that in Lumerical. A single point source, emitting a Gaussian pulse with a frequency width of  $\Delta f = 0.002(c/\Lambda)$ , is randomly embedded in a

dielectric rod at the interface. The central frequency of this optical pulse follows a straight trajectory along the chiral edge mode,  $f_{\text{center}} = (0.06\delta + 0.2086)(c/\Lambda)$ . The source excites modes with an electric field parallel to the dielectric rod. A monitor is placed inside another dielectric rod at the junction interface to analyze the response for  $10^4$  time units after the source has turned off. The 2D computational cell has a resolution of 32 and dimensions of  $(N + 7, 26)$ , where  $N$  is the number of periods on each side. The boundary layers perpendicular to the  $y$ -axis are phase matching layers of thickness 2, while those normal to the  $x$ -axis are adiabatic absorbers of thickness 7. The periodic lattices submerge into the absorbers.

**Lasing simulation** – For lasing simulations in Lumerical FDTD, the heterojunction is constructed similarly but we use a realistic geometry with  $\Lambda = 366\ \text{nm}$  since the calculations are nonlinear. The lower grating is still a dielectric with the refractive index 2.73 while the upper grating now is modeled by a four-level two-electron material [40], akin to what is depicted in Fig. 5B. In this gain material, the transition wavelengths are  $\lambda_s = 1.5\ \mu\text{m}$  and  $\lambda_e = 0.85\ \mu\text{m}$ , the damping coefficients are  $\gamma_a = \gamma_b = 10^{13}\ \text{Hz}$ , the lifetimes of different decay channels are  $t_{30} = t_{21} = 3 \times 10^{-10}\ \text{s}$  and  $t_{32} = t_{10} = 10^{-13}\ \text{s}$ , and the electron population density is  $1 \times 10^{23}\ \text{m}^{-3}$ . The heterojunction is continuously pumped by a spatial-Gaussian beam with wavelength  $\lambda_e$  and waist radius  $2\ \mu\text{m}$ , located  $2.2\ \mu\text{m}$  above the system. The signals are recorded and analyzed by 10 time monitors located  $0.5\ \mu\text{m}$  below the system. The heterojunction in these simulations has 300 periods, corresponding to a length of approximately  $110\ \mu\text{m}$ . The simulations run for 360 ps at 300 K. The mesh for finite-difference calculation has the maximum mesh step  $0.006\ \mu\text{m}$  along the  $x$  direction and 60 mesh cells per wavelength along the  $y$  direction.

- 
- [1] K. V. Klitzing, G. Dorda, and M. Pepper, New method for high-accuracy determination of the fine-structure constant based on quantized hall resistance, *Phys. Rev. Lett.* **45**, 494 (1980).
- [2] R. B. Laughlin, Quantized hall conductivity in two dimensions, *Phys. Rev. B* **23**, 5632 (1981).
- [3] D. J. Thouless, M. Kohmoto, M. P. Nightingale, and M. den Nijs, Quantized hall conductance in a two-dimensional periodic potential, *Phys. Rev. Lett.* **49**, 405 (1982).
- [4] D. J. Thouless, Quantization of particle transport, *Phys. Rev. B* **27**, 6083 (1983).
- [5] P. Wang, Q. Fu, R. Peng, Y. V. Kartashov, L. Torner, V. V. Konotop, and F. Ye, Two-dimensional thouless pumping of light in photonic moiré lattices, *Nat. Commun.* **13**, 6738 (2022).
- [6] R. Citro and M. Aidelsburger, Thouless pumping and topology, *Nat. Rev. Phys.* **5**, 87–101 (2023).
- [7] K. Yang, Q. Fu, H. C. Prates, P. Wang, Y. V. Kartashov, V. V. Konotop, and F. Ye, Observation of Thouless pumping of light in quasiperiodic photonic crystals, *Proc. Natl. Acad. Sci. U.S.A.* **121**, e2411793121 (2024).
- [8] Y.-K. Sun, Z.-L. Shan, Z.-N. Tian, Q.-D. Chen, and X.-L. Zhang, Two-dimensional non-Abelian Thouless pump, *Nat. Commun.* **15**, 9311 (2024).
- [9] S. P. Villani, M. Campetella, P. Barone, and F. Mauri, Giant piezoelectricity driven by thouless pump in conjugated polymers, *npj Comput. Mater.* **10**, 81 (2024).
- [10] W. Song, O. You, J. Sun, S. Wu, C. Chen, C. Huang, K. Qiu, S. Zhu, S. Zhang, and T. Li, Fast topological pumps via quantum metric engineering on photonic chips, *Sci. Adv.* **10**, eadn5028 (2024).
- [11] K. Viebahn, A.-S. Walter, E. Bertok, Z. Zhu, M. Gächter, A. A. Aligia, F. Heidrich-Meisner, and T. Esslinger, Interactions enable thouless pumping in a nonsliding lattice, *Phys. Rev. X* **14**, 021049 (2024).

- [12] S. Ravets, N. Pernet, N. Mostaan, N. Goldman, and J. Bloch, Thouless pumping in a driven-dissipative Kerr resonator array (2024), arXiv:2407.02627.
- [13] S. Athanasiou, I. E. Nielsen, M. M. Wauters, and M. Burdello, Thouless pumping in Josephson junction arrays, *SciPost Phys.* **16**, 083 (2024).
- [14] Y. Liu, Y.-R. Zhang, Y.-H. Shi, T. Liu, C. Lu, Y.-Y. Wang, H. Li, T.-M. Li, C.-L. Deng, S.-Y. Zhou, T. Liu, J.-C. Zhang, G.-H. Liang, Z.-Y. Mei, W.-G. Ma, H.-T. Liu, Z.-H. Liu, C.-T. Chen, K. Huang, X. Song, S. P. Zhao, Y. Tian, Z. Xiang, D. Zheng, F. Nori, K. Xu, and H. Fan, Interplay between disorder and topology in Thouless pumping on a superconducting quantum processor, *Nat. Commun.* **16**, 108 (2025).
- [15] H. S. Nguyen, F. Dubois, T. Deschamps, S. Cuffe, A. Pardon, J.-L. Leclercq, C. Seassal, X. Letartre, and P. Viktorovitch, Symmetry Breaking in Photonic Crystals: On-Demand Dispersion from Flatband to Dirac Cones, *Phys. Rev. Lett.* **120**, 066102 (2018).
- [16] D. X. Nguyen, X. Letartre, E. Drouard, P. Viktorovitch, H. C. Nguyen, and H. S. Nguyen, Magic configurations in moiré superlattice of bilayer photonic crystals: Almost-perfect flatbands and unconventional localization, *Phys. Rev. Res.* **4**, L032031 (2022).
- [17] X. Letartre, S. Mazauric, S. Cuffe, T. Benyattou, H. S. Nguyen, and P. Viktorovitch, Analytical non-Hermitian description of photonic crystals with arbitrary lateral and transverse symmetry, *Phys. Rev. A* **106**, 033510 (2022).
- [18] S. G. Johnson and J. D. Joannopoulos, Block-iterative frequency-domain methods for Maxwell's equations in a planewave basis, *Opt. Express* **8**, 173 (2001).
- [19] R. Resta and D. Vanderbilt, Theory of polarization: A modern approach, in *Physics of Ferroelectrics: A Modern Perspective* (Springer Berlin Heidelberg, Berlin, Heidelberg, 2007) pp. 31–68.
- [20] J. K. Asbóth, L. Oroszlány, and A. Pályi, *A Short Course on Topological Insulators* (Springer International Publishing, 2016).
- [21] M. Blanco de Paz, M. A. J. Herrera, P. Arroyo Huidobro, H. Alaeian, M. G. Vergniory, B. Bradlyn, G. Giedke, A. García-Etxarri, and D. Bercioux, Energy density as a probe of band representations in photonic crystals, *J. Phys. Condens. Matter* **34**, 314002 (2022).
- [22] Lumerical Inc.
- [23] K. Y. Lee, S. Yoon, S. H. Song, and J. W. Yoon, Topological beaming of light, *Science Advances* **8**, 10.1126/sciadv.add8349 (2022).
- [24] T. Uemura, Y. Moritake, T. Yoda, H. Chiba, Y. Tanaka, M. Ono, E. Kuramochi, and M. Notomi, Photonic topological phase transition induced by material phase transition, *Sci. Adv.* **10**, eadp7779 (2024).
- [25] C. Li, X. Hu, W. Gao, Y. Ao, S. Chu, H. Yang, and Q. Gong, Thermo-optical Tunable Ultracompact Chip-Integrated 1D Photonic Topological Insulator, *Adv. Opt. Mater.* **6**, 1701071 (2017).
- [26] D. Leykam, S. Mittal, M. Hafezi, and Y. D. Chong, Reconfigurable topological phases in next-nearest-neighbor coupled resonator lattices, *Phys. Rev. Lett.* **121**, 023901 (2018).
- [27] Z. A. Kudyshev, A. V. Kildishev, A. Boltasseva, and V. M. Shalaev, Tuning topology of photonic systems with transparent conducting oxides, *ACS Photonics* **6**, 1922–1930 (2019).
- [28] T. Cao, L. Fang, Y. Cao, N. Li, Z. Fan, and Z. Tao, Dynamically reconfigurable topological edge state in phase change photonic crystals, *Sci. Bull.* **64**, 814–822 (2019).
- [29] F. Tian, J. Zhou, Q. Wang, and Z. Liu, Tunable topological phase transition in the telecommunication wavelength, *Opt. Mater. Express* **13**, 1571 (2023).
- [30] J. Han, F. Liang, Y. Zhao, X. Wang, D. Zhao, and B.-Z. Wang, Reconfigurable topological wave routing based on tunable valley kink states and valley-polarized chiral edge states, *Opt. Express* **32**, 26819 (2024).
- [31] Z. Quan and J. Wang, Photonic crystal topological interface state modulation for nonvolatile optical switching, *Photon. Res.* **12**, 2178 (2024).
- [32] J. Faneca, L. Trimby, I. Zeimpekis, M. Delaney, D. W. Hewak, F. Y. Gardes, C. D. Wright, and A. Baldycheva, On-chip sub-wavelength Bragg grating design based on novel low loss phase-change materials, *Opt. Express* **28**, 16394 (2020).
- [33] O. Hemmatyar, S. Abdollahramezani, I. Zeimpekis, S. Lepeshov, A. Krasnok, A. I. Khan, K. M. Neilson, C. Teichrib, T. Brown, E. Pop, D. W. Hewak, M. Wuttig, A. Alu, O. L. Muskens, and A. Adibi, Enhanced metasurfaces using advanced phase-change materials (2021), arXiv:2107.12159.
- [34] P. Moitra, Y. Wang, X. Liang, L. Lu, A. Poh, T. W. Mass, R. E. Simpson, A. I. Kuznetsov, and R. Paniagua-Dominguez, Programmable wavefront control in the visible spectrum using low-loss chalcogenide phase-change metasurfaces, *Adv. Mater.* **35**, 2205367 (2023).
- [35] P. St-Jean, V. Goblot, E. Galopin, A. Lemaitre, T. Ozawa, L. Le Gratiet, I. Sagnes, J. Bloch, and A. Amo, Lasing in topological edge states of a one-dimensional lattice, *Nat. Photonics* **11**, 651 (2017).
- [36] Y. Ota, R. Katsumi, K. Watanabe, S. Iwamoto, and Y. Arakawa, Topological photonic crystal nanocavity laser, *Commun. Phys.* **1**, 86 (2018).
- [37] H. Zhao, P. Miao, M. H. Teimourpour, S. Malzard, R. El-Ganainy, H. Schomerus, and L. Feng, Topological hybrid silicon microlasers, *Nat. Commun.* **9**, 981 (2018).
- [38] C. Han, M. Lee, S. Callard, C. Seassal, and H. Jeon, Lasing at topological edge states in a photonic crystal L3 nanocavity dimer array, *Light Sci. Appl.* **8**, 40 (2019).
- [39] Y. Gong, S. Wong, A. J. Bennett, D. L. Huffaker, and S. S. Oh, Topological Insulator Laser Using Valley-Hall Photonic Crystals, *ACS Photonics* **7**, 2089–2097 (2020).
- [40] S.-H. Chang and A. Taflove, Finite-difference time-domain model of lasing action in a four-level two-electron atomic system, *Opt. Express* **12**, 3827 (2004).
- [41] S. Cuffe, F. Dubois, M. S. R. Huang, D. Li, R. Zia, X. Letartre, P. Viktorovitch, and H. S. Nguyen, Tailoring the local density of optical states and directionality of light emission by symmetry breaking, *IEEE J. Sel. Top. Quantum Electron.* **25**, 1 (2019).
- [42] M. C. Wu, O. Solgaard, and J. E. Ford, Optical mems for lightwave communication, *J. Light. Technol.* **24**, 4433–4454 (2006).
- [43] Q. Liang, D. Zhang, G. Coppola, Y. Wang, S. Wei, and Y. Ge, Multi-dimensional MEMS/micro sensor for force and moment sensing: A review, *IEEE Sens. J.* **14**, 2643 (2014).
- [44] F. Chollet, Devices based on co-integrated mems actuators and optical waveguide: A review, *Micromachines* **7**, 18 (2016).

- [45] Z. Ren, Y. Chang, Y. Ma, K. Shih, B. Dong, and C. Lee, Leveraging of mems technologies for optical metamaterials applications, *Adv. Opt. Mater.* **8**, 1900653 (2020).
- [46] H. Tang, B. Lou, F. Du, G. Gao, M. Zhang, X. Ni, E. Hu, A. Yacoby, Y. Cao, S. Fan, and E. Mazur, On-chip multidimensional dynamic control of twisted moiré photonic crystal for smart sensing and imaging (2023), arXiv:2312.09089.
- [47] J. Wen, J. Jiang, J. Ma, S. Feng, Q. Gong, W. Xiao, X. Lian, and L. Wang, The state-of-the-art phase-change integrated photonic devices with electrically driven microheaters, *IEEE Trans. Electron Devices* **71**, 955–964 (2024).
- [48] H. Taghinejad, S. Abdollahramezani, A. A. Eftekhar, T. Fan, A. H. Hosseinnia, O. Hemmatyar, A. E. Dorche, A. Gallmon, and A. Adibi, ITO-based microheaters for reversible multi-stage switching of phase-change materials: towards miniaturized beyond-binary reconfigurable integrated photonics, *Opt. Express* **29**, 20449 (2021).
- [49] J. Zheng, Z. Fang, C. Wu, S. Zhu, P. Xu, J. K. Doylend, S. Deshmukh, E. Pop, S. Dunham, M. Li, and A. Majumdar, Nonvolatile electrically reconfigurable integrated photonic switch enabled by a silicon PIN diode heater, *Adv. Mater.* **32**, 2001218 (2020).
- [50] R. Chen, Z. Fang, C. Perez, F. Miller, K. Kumari, A. Saxena, J. Zheng, S. J. Geiger, K. E. Goodson, and A. Majumdar, Non-volatile electrically programmable integrated photonics with a 5-bit operation, *Nat. Commun.* **14**, 3465 (2023).
- [51] Z. Fang, R. Chen, J. Zheng, A. I. Khan, K. M. Neilson, S. J. Geiger, D. M. Callahan, M. G. Moebius, A. Saxena, M. E. Chen, C. Rios, J. Hu, E. Pop, and A. Majumdar, Ultra-low-energy programmable non-volatile silicon photonics based on phase-change materials with graphene heaters, *Nat. Nanotechnol.* **17**, 842 (2022).
- [52] Y. E. Kraus, Z. Ringel, and O. Zilberberg, Four-Dimensional Quantum Hall Effect in a Two-Dimensional Quasicrystal, *Phys. Rev. Lett.* **111**, 226401 (2013).
- [53] M. Lohse, C. Schweizer, H. M. Price, O. Zilberberg, and I. Bloch, Exploring 4D quantum Hall physics with a 2D topological charge pump, *Nature* **553**, 55–58 (2018).
- [54] M. Fujimoto, H. Koschke, and M. Koshino, Topological charge pumping by a sliding moiré pattern, *Phys. Rev. B* **101**, 041112 (2020).
- [55] Y. Su and S.-Z. Lin, Topological sliding moiré heterostructure, *Phys. Rev. B* **101**, 041113 (2020).
- [56] P. Hu, H.-W. Wu, P. Xie, Y. Zhuo, W. Sun, Z. Sheng, and Y. Pan, Hearing the dynamical Floquet-Thouless pump of a sound pulse, *Phys. Rev. B* **110**, 085137 (2024).
- [57] W. Liu, Y. Ke, and C. Lee, Shortcuts to adiabatic thouless pumping (2024), arXiv:2401.17081.
- [58] S. A. R. Horsley and J. B. Pendry, Quantum electrodynamics of time-varying gratings, *Proc. Natl. Acad. Sci. U.S.A.* **120**, e2302652120 (2023).
- [59] S. A. R. Horsley and J. B. Pendry, Traveling wave amplification in stationary gratings, *Phys. Rev. Lett.* **133**, 156903 (2024).
- [60] O. Boada, A. Celi, J. I. Latorre, and M. Lewenstein, Quantum simulation of an extra dimension, *Phys. Rev. Lett.* **108**, 133001 (2012).
- [61] L. Yuan, Q. Lin, M. Xiao, and S. Fan, Synthetic dimension in photonics, *Optica* **5**, 1396 (2018).
- [62] E. Lustig and M. Segev, Topological photonics in synthetic dimensions, *Adv. Opt. Photon.* **13**, 426 (2021).
- [63] M. Ehrhardt, S. Weidemann, L. J. Maczewsky, M. Heinrich, and A. Szameit, A perspective on synthetic dimensions in photonics, *Laser Photonics Rev.* **17**, 2200518 (2023).
- [64] T. Grass, D. Bercioux, U. Bhattacharya, M. Lewenstein, H. S. Nguyen, and C. Weitenberg, Colloquium: Synthetic quantum matter in non-standard geometries (2024), arXiv:2407.06105.
- [65] K. Y. Lee, K. W. Yoo, S. Cheon, W.-J. Joo, J. W. Yoon, and S. H. Song, Synthetic topological nodal phase in bilayer resonant gratings, *Phys. Rev. Lett.* **128**, 053002 (2022).
- [66] K. Y. Lee, K. W. Yoo, F. Monticone, and J. W. Yoon, Dirac bilayer metasurfaces as an inverse gires-tournois etalon (2023), arXiv:2311.08766 [physics.optics].
- [67] G. Montambaux, F. Piéchon, J.-N. Fuchs, and M. O. Goerbig, Merging of Dirac points in a two-dimensional crystal, *Phys. Rev. B* **80**, 153412 (2009).
- [68] M. Goerbig and G. Montambaux, Dirac fermions in condensed matter and beyond, in *Dirac Matter* (Springer International Publishing, 2017) pp. 25–53.
- [69] B. A. Bernevig, *Topological Insulators and Topological Superconductors* (Princeton University Press, 2013).
- [70] P.-O. Löwdin, A Note on the Quantum-Mechanical Perturbation Theory, *J. Chem. Phys.* **19**, 1396 (1951).
- [71] R. Winkler, *Spin—Orbit Coupling Effects in Two-Dimensional Electron and Hole Systems* (Springer Berlin Heidelberg, 2003).
- [72] M. Delaney, I. Zeimpekis, D. Lawson, D. W. Hewak, and O. L. Muskens, A new family of ultralow loss reversible phase-change materials for photonic integrated circuits: Sb<sub>2</sub>S<sub>3</sub> and Sb<sub>2</sub>Se<sub>3</sub>, *Advanced Functional Materials* **30**, 2002447 (2020).
- [73] Z. Fang, J. Zheng, A. Saxena, J. Whitehead, Y. Chen, and A. Majumdar, Non-volatile reconfigurable integrated photonics enabled by broadband low-loss phase change material, *Adv. Opt. Mater.* **9**, 2002049 (2021).
- [74] Y. Gutiérrez, A. P. Ovyvan, G. Santos, D. Juan, S. A. Rosales, J. Junquera, P. García-Fernández, S. Dico-rato, M. M. Giangregorio, E. Dilonardo, F. Palumbo, M. Modreanu, J. Resl, O. Ishchenko, G. Garry, T. Jonuzi, M. Georghe, C. Cobianu, K. Hingerl, C. Cobet, F. Moreno, W. H. P. Pernice, and M. Losurdo, Inter-laboratory study on Sb<sub>2</sub>S<sub>3</sub> interplay between structure, dielectric function, and amorphous-to-crystalline phase change for photonics, *iScience* **25**, 104377 (2022).
- [75] H. Liu, W. Dong, H. Wang, L. Lu, Q. Ruan, Y. S. Tan, R. E. Simpson, and J. K. W. Yang, Rewritable color nanoprnts in antimony trisulfide films, *Sci. Adv.* **6**, eabb7171 (2020).
- [76] C. Laprais, C. Zrounba, J. Bouvier, N. Blanchard, M. Bugnet, A. Gassenq, Y. Gutiérrez, S. Vazquez-Miranda, S. Espinoza, P. Thiesen, R. Bourrellier, A. Benamrouche, N. Baboux, G. Saint-Girons, L. Berguiga, and S. Cueff, Reversible single-pulse laser-induced phase change of Sb<sub>2</sub>S<sub>3</sub> thin films: Multi-physics modeling and experimental demonstrations, *Adv. Opt. Mater.* , 2401214 (2024).
- [77] A. Taute, S. Al-Jibouri, C. Laprais, S. Monfray, J. Lumeau, A. Moreau, X. Letartre, N. Baboux, G. Saint-Girons, L. Berguiga, and S. Cueff, A simple method for programming and analyzing multilevel crystallization states in phase-change materials thin film (2023), arXiv:2306.17631.

- [78] S. Abdollahramezani, O. Hemmatyar, M. Taghinejad, H. Taghinejad, K. Alex, A. A. Eftekhar, C. Teichrib, S. Deshmukh, M. A. El-Sayed, E. Pop, M. Wuttig, A. Alù, W. Cai, and A. Adibi, Electrically driven re-programmable phase-change metasurface reaching 80% efficiency, *Nat. Commun.* **13**, 1696 (2022).
- [79] H. Tang, Y. Wang, X. Ni, K. Watanabe, T. Taniguchi, P. Jarillo-Herrero, S. Fan, E. Mazur, A. Yacoby, and Y. Cao, On-chip multi-degree-of-freedom control of two-dimensional materials, *Nature* **632**, 1038–1044 (2024).
- [80] A. F. Oskooi, D. Roundy, M. Ibanescu, P. Bermel, J. Joannopoulos, and S. G. Johnson, Meep: A flexible free-software package for electromagnetic simulations by the FDTD method, *Comput. Phys. Commun.* **181**, 687 (2010).
- [81]  $\Theta(x)$  is the Heaviside function.
- [82] As the spectral gap has not been optimized in this example, the range of filtering wavelength can certainly be further increased.
- [83] D.-H.-M. Nguyen, C. Devescovi, D. X. Nguyen, H. S. Nguyen, and D. Bercioux, Fermi arc reconstruction in synthetic photonic lattice, *Phys. Rev. Lett.* **131**, 053602 (2023).

## ACKNOWLEDGMENTS

We warmly acknowledge Pierre Viktorovitch for having participated in the early stage of the project. We are grateful to Pierre Delplace, David Carpentier, Sébastien Cueff, and Alexander Cerjan for fruitful discussions. This work was granted access to the HPC resources of PMCS2I (Pôle de Modélisation et de Calcul en Sciences de l'Ingénieur de l'Information) of École Centrale de Lyon, Écully, France. The authors acknowledge the technical and human support pro-

vided by the DIPC Supercomputing Center.

**Funding:** This work was supported by Spanish Ministerio de Ciencia e Innovación grant PRE2021-097126 (DHMN)

Deutsche Forschungsgemeinschaft (DFG, German Research Foundation, project numbers 447948357 and 440958198), Sino-German Center for Research Promotion (Project M-0294), the ERC (Consolidator Grant 683107/TempoQ), German Ministry of Education and Research (Project QuKuK, BMBF Grant No. 16KIS1618K), and the EIN Quantum NRW (HCN)

Brown Theoretical Physics Center, Institute for Basic Science in Korea through the Project IBS-R024-D1 (DXN)

French National Research Agency grant ANR-17-CE24-0020, IDEXLYON from Université de Lyon, Scientific Breakthrough project TORE within the Programme Investissements d'Avenir grant ANR-19-IDEX-0005 (TL, XL, HSN)

French National Research Agency (ANR) under the project POLAROID (ANR-24-CE24-7616-01) (HSN)

Transnational Common Laboratory *QuantumChemPhys* and Department of Education of the Basque Government through the project PIBA 2023 1 0007 (STRAINER) (DB)

### Author contributions:

Conceptualization: HSN, DXN, HCN, DHMN, DB

Investigation: DHMN, HCN, TL

Methodology: XV, HCN, DXN

Software: ED, XV, TL

Supervision: HSN, DB

Writing — original draft: HCN

Writing — review & editing: DHMN, DB, HSN, DXN

**Competing interests:** The authors declare that they have no competing interests.

**Data and materials availability:** All data needed to evaluate the conclusions in the paper are present in the paper and/or the Supplementary Materials.

**SUPPLEMENTAL MATERIAL:**  
**Reconfigurable topological lasing through Thouless pumping in  
 bilayer photonic crystal**

D.-H.-Minh Nguyen\*, Dung Xuan Nguyen\*, Hai-Chau Nguyen, Thibaud Louvet, Emmanuel Drouard, Xavier Letartre,  
 Dario Bercioux\*, Hai Son Nguyen\*

**CONTENTS**

I. Effective model	1
A. Derivation	1
B. Symmetries	5
C. Dispersion of homo-bilayer grating	6
II. Two-band models	7
A. Lower and upper gap	7
B. Middle gap	9
1. Emergence and merging of Dirac points	10
2. Emergence and merging of gapped Dirac valleys	10
III. Temperature dependence of antimony trisulfide	11
IV. Guided transmission for broadband filtering	12
A. Design	12
B. Guided transmission	13
C. Advantages	13
V. Additional information about the lasing simulation	13
VI. Edge state from effective model	14
VII. Supplemental Figures	14

**I. EFFECTIVE MODEL**

In this section, we present the derivation of the effective Hamiltonian, the symmetry operators associated with this Hamiltonian, and some insights into its spectrum in a special case where the two gratings are identical.

**A. Derivation**

The system consists of two gratings with the same period  $\Lambda$  separated by distance  $D$ . The confinement of electromagnetic waves within each grating is considerably analogous to the problem of an electron in a finite quantum well. Hence, for simplicity, we will investigate how the optical modes in each grating are effectively described and then phenomenologically add the evanescent coupling between modes in different gratings.

We consider a symmetric grating of dielectric constant  $\varepsilon_s$  in the air with thickness  $H$  and width  $L$ , the spatial dielectric function is given by  $\varepsilon(x, z) = [\varepsilon(x) - 1]f_e(z) + 1$ , where the relative dielectric constant of the grating with respect to the environment is a periodic function with the period  $\Lambda$  and

$$\varepsilon(x) = \begin{cases} \varepsilon_s & \text{for } -L/2 < x < L/2 \\ 1 & \text{for } -\Lambda/2 < x < -L/2 \text{ or } L/2 < x < \Lambda/2 \end{cases}, \quad (\text{S1})$$

and  $f_e(z) = \Theta(z + W/2) - \Theta(z - W/2)$  [81]. As  $\varepsilon(x) - 1$  is a periodic function, we can write its Fourier expansion as  $\varepsilon(x) - 1 = \sum_{n=-\infty}^{+\infty} \xi_n e^{i2\pi n x/\Lambda}$ , which gives

$$\varepsilon(x, z) = \xi_0 f_e(z) + 1 + \sum_{n \neq 0} \xi_n(z) e^{i\frac{2\pi n}{\Lambda} x} = \bar{\varepsilon}(z) + \sum_{n \neq 0} \xi_n(z) e^{i\frac{2\pi n}{\Lambda} x}, \quad \xi_n(z) = \xi_n f_e(z). \quad (\text{S2})$$

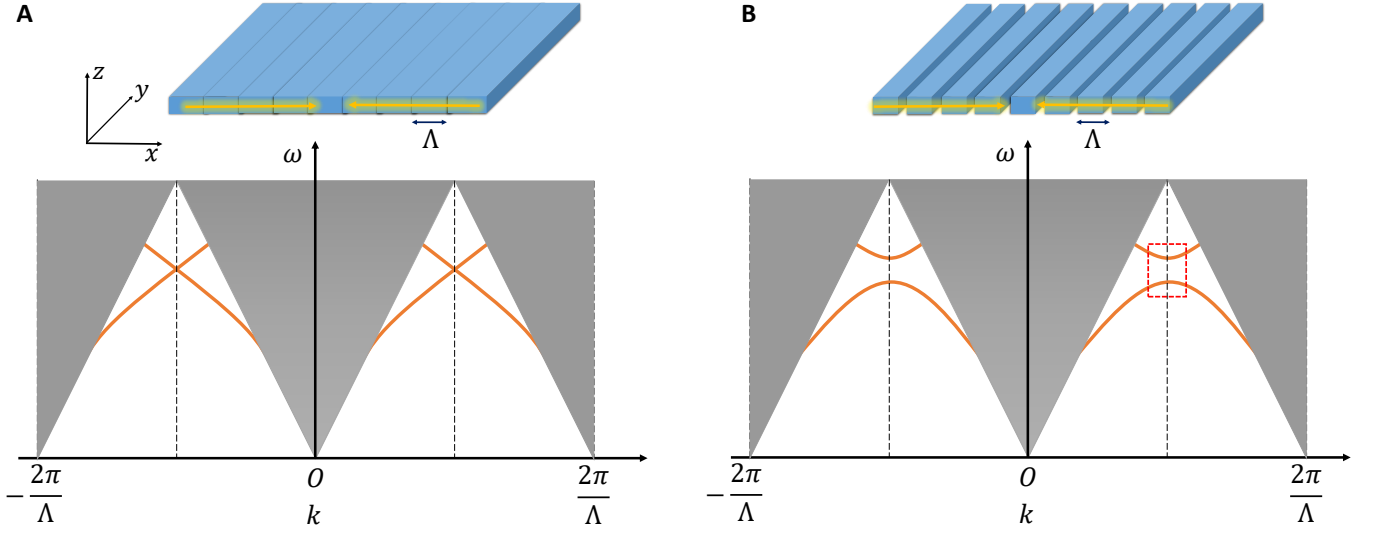


FIG. S1. Dispersion of the lowest guided mode in (a) a homogeneous waveguide with infinitesimal periodic modulation of dielectric, and (b) a dielectric grating. The red dashed box indicates the region where the effective model is valid.

The electromagnetic field of this system is governed by the Maxwell's equations

$$\begin{aligned} \nabla \cdot \mathbf{H} &= 0, & \nabla \times \mathbf{H} &= \varepsilon_0 \varepsilon \frac{\partial \mathbf{E}}{\partial t}, \\ \nabla \cdot (\varepsilon \mathbf{E}) &= 0, & \nabla \times \mathbf{E} &= -\mu_0 \frac{\partial \mathbf{H}}{\partial t}. \end{aligned}$$

Since the system is uniform and infinite along the  $y$  direction, we can decompose the solutions at momentum  $k_y = 0$  into two sets of modes: transverse electric (TE) modes with  $E_x = E_z = 0$ , and transverse magnetic (TM) modes with  $H_x = H_z = 0$ . These modes have fields' strengths distribute uniformly along the  $y$  direction. In our case, we are only interested in TE modes but a theory for the TM ones can be developed similarly. The Maxwell's equations are consequently reduced to the wave equation

$$\frac{\partial^2 E_y}{\partial z^2} + \frac{\partial^2 E_y}{\partial x^2} = -\varepsilon(x, z) \frac{\omega^2}{c^2} E_y. \quad (\text{S3})$$

Due to the discrete translation symmetry of the grating, we employ the Bloch theorem to write the electric field in terms of plane waves

$$E_y(\mathbf{r}) = \sum_n C_n(z) e^{i(k_x + K_n)x}, \quad \text{with } K_n = \frac{2\pi n}{\Lambda}. \quad (\text{S4})$$

Inserting this expression into the wave equation, we get

$$\sum_n e^{i(k_x + K_n)x} \left[ \frac{\partial^2}{\partial z^2} + \bar{\varepsilon}(z) \frac{\omega^2}{c^2} - (k_x + K_n)^2 \right] C_n(z) = -\frac{\omega^2}{c^2} \sum_{n, l \neq 0} \xi_l(z) e^{i(k_x + K_{n+l})x} C_n(z). \quad (\text{S5})$$

Multiply two sides with  $e^{-i(k_x + K_m)x}$  and integrate over  $x$ , we get

$$\left[ \frac{\partial^2}{\partial z^2} + \bar{\varepsilon}(z) \frac{\omega^2}{c^2} - (k_x + K_n)^2 \right] C_n(z) = -\frac{\omega^2}{c^2} \sum_{l \neq n} \xi_{n-l}(z) C_l(z). \quad (\text{S6})$$

We divide the plane wave basis into two sets: basic waves  $\mathcal{B}$  and others  $\mathcal{O}$ . The basic waves are those that contribute most to the modes of interest. We impose our first approximation by assuming that the basic waves have the form  $C_n(z) = E_{0y}(z) C_n$  for  $n \in \mathcal{B}$ , where  $E_{0y}(z)$  is the envelop function of the lowest-frequency guided TE modes in a homogeneous slab described by the dielectric function  $\bar{\varepsilon}(z)$ . We have

$$\frac{\partial^2 E_{0y}(z)}{\partial z^2} - (k_x + K_n)^2 E_{0y}(z) = -\bar{\varepsilon}(z) \frac{\omega^2}{c^2} E_{0y}(z). \quad (\text{S7})$$

Here,  $\omega$  and  $E_{0y}(z)$  vary with respect to the momentum  $k_x + K_n$ . Since in the case of grating, we only work with a small range of momentum around a high-symmetry point  $k_x + K_n = \tilde{K}$ , we assume that  $\omega$  and  $E_{0y}(z)$  are  $k$ -independent and are values at this point  $\tilde{K}$ . Thus, these two quantities are now determined via the wave equation

$$\frac{\partial^2 E_{0y}(z)}{\partial z^2} - \tilde{K}^2 E_{0y}(z) = -\bar{\varepsilon}(z) \frac{\omega_{\tilde{K}}^2}{c^2} E_{0y}(z). \quad (\text{S8})$$

Combining this equation with the wave equation for electromagnetic waves in the grating, we arrive at

$$\left[ \bar{\varepsilon}(z) \frac{\omega^2 - \omega_{\tilde{K}}^2}{c^2} + \tilde{K}^2 - (k_x + K_n)^2 \right] E_{0y}(z) C_n = -\frac{\omega^2}{c^2} \left[ E_{0y}(z) \sum_{l \in \mathcal{B}, l \neq n} \xi_{n-l}(z) C_l + \sum_{u \in \mathcal{O}} \xi_{n-u}(z) C_u(z) \right]. \quad (\text{S9})$$

Then, multiplying both sides by  $E_{0y}^*(z)$  and taking integration over  $z$  yields

$$\left\{ \omega^2 - \omega_{\tilde{K}}^2 + \frac{c^2}{\bar{n}_0^2} \left[ \tilde{K}^2 - (k_x + K_n)^2 \right] \right\} C_n = -\alpha \omega^2 \sum_{l \in \mathcal{B}, l \neq n} \xi_{n-l} C_l - \omega^2 \sum_{u \in \mathcal{O}} \xi_{n-u} \int_{-\infty}^{+\infty} dz E_{0y}^*(z) C_u(z) f_e(z) \quad (\text{S10})$$

with  $\bar{n}_0^2 = \int_{-\infty}^{+\infty} |E_{0y}(z)|^2 \bar{\varepsilon}(z) dz$  and  $\alpha = \int_{-\infty}^{+\infty} |E_{0y}(z)|^2 f_e(z) dz$ . We choose the point of interest  $\tilde{K} = K_1/2$ , notate  $\omega_{\tilde{K}} = \omega_0$ , and consider two basic waves corresponding to  $n = 0$  and  $n = -1$ , which gives two coupled equations

$$\left\{ \omega^2 - \omega_0^2 + \frac{c^2}{\bar{n}_0^2} \left[ \frac{K_1^2}{4} - (k_x + K_{-1})^2 \right] \right\} C_{-1} = -\alpha \omega^2 \xi_{-1} C_0 - \omega^2 \sum_{u \neq 0, -1} \xi_{-1-u} \int_{-\infty}^{+\infty} dz E_{0y}^*(z) C_u(z) f_e(z), \quad (\text{S11a})$$

$$\left\{ \omega^2 - \omega_0^2 + \frac{c^2}{\bar{n}_0^2} \left( \frac{K_1^2}{4} - k_x^2 \right) \right\} C_0 = -\alpha \omega^2 \xi_1 C_{-1} - \omega^2 \sum_{u \neq 0, -1} \xi_{-u} \int_{-\infty}^{+\infty} dz E_{0y}^*(z) C_u(z) f_e(z). \quad (\text{S11b})$$

Define  $k = k_x - K_1/2$  and neglect the interaction with higher-order modes ( $u \neq 0, -1$ ), we obtain

$$\left\{ \omega^2 - \omega_0^2 + \frac{c^2}{\bar{n}_0^2} \left[ \frac{K_1^2}{4} - \left( k - \frac{K_1}{2} \right)^2 \right] \right\} C_{-1} = -\alpha \omega^2 \xi_{-1} C_0 \Rightarrow \left[ \omega^2 - \omega_0^2 - \frac{c^2}{\bar{n}_0^2} (k^2 - K_1 k) \right] C_{-1} = -\alpha \omega^2 \xi_{-1} C_0, \quad (\text{S12a})$$

$$\left\{ \omega^2 - \omega_0^2 + \frac{c^2}{\bar{n}_0^2} \left[ \frac{K_1^2}{4} - \left( k + \frac{K_1}{2} \right)^2 \right] \right\} C_0 = -\alpha \omega^2 \xi_1 C_{-1} \Rightarrow \left[ \omega^2 - \omega_0^2 - \frac{c^2}{\bar{n}_0^2} (k^2 + K_1 k) \right] C_0 = -\alpha \omega^2 \xi_1 C_{-1}. \quad (\text{S12b})$$

If the periodic modulation in the dielectric function of the grating is sufficiently weak, we can considerably simplify these equations by assuming that  $|\omega - \omega_0| \ll \omega_0$  and neglecting the term of  $(\omega - \omega_0)\xi_{\pm 1}$ . The equations then become

$$\left[ \omega - \omega_0 - \frac{c^2}{2\bar{n}_0^2 \omega_0} (k^2 - K_1 k) \right] C_{-1} \approx -\frac{\alpha \omega_0 \xi_{-1}}{2} C_0, \quad (\text{S13a})$$

$$\left[ \omega - \omega_0 - \frac{c^2}{2\bar{n}_0^2 \omega_0} (k^2 + K_1 k) \right] C_0 \approx -\frac{\alpha \omega_0 \xi_1}{2} C_{-1}. \quad (\text{S13b})$$

Rewriting these two equations in matrix form gives us the effective model of a single grating

$$\omega_0 + \frac{c^2}{2\bar{n}_0^2 \omega_0} k^2 + \begin{pmatrix} \bar{v}k & U \\ U^* & -\bar{v}k \end{pmatrix} \begin{pmatrix} C_0 \\ C_{-1} \end{pmatrix} = \omega \begin{pmatrix} C_0 \\ C_{-1} \end{pmatrix} \quad (\text{S14})$$

with  $\bar{v} = \frac{\pi c^2}{\bar{n}_0^2 \omega_0 \Lambda}$  and  $U = -\frac{\alpha \omega_0 \xi_1}{2}$ . Owing to the inversion symmetry along the  $x$  direction of the dielectric function, we have  $U = U^*$ . For simplicity, we neglect the  $k$ -quadratic term as it has no effect on the topological properties of the spectrum — the wave equation can thus be written as an eigen-equation  $H_{\text{mono}}(k)\Psi(k) = \omega_k \Psi(k)$  with the operator

$$H(k) = \omega_0 + \begin{pmatrix} \bar{v}k & U \\ U & -\bar{v}k \end{pmatrix} \quad (\text{S15})$$

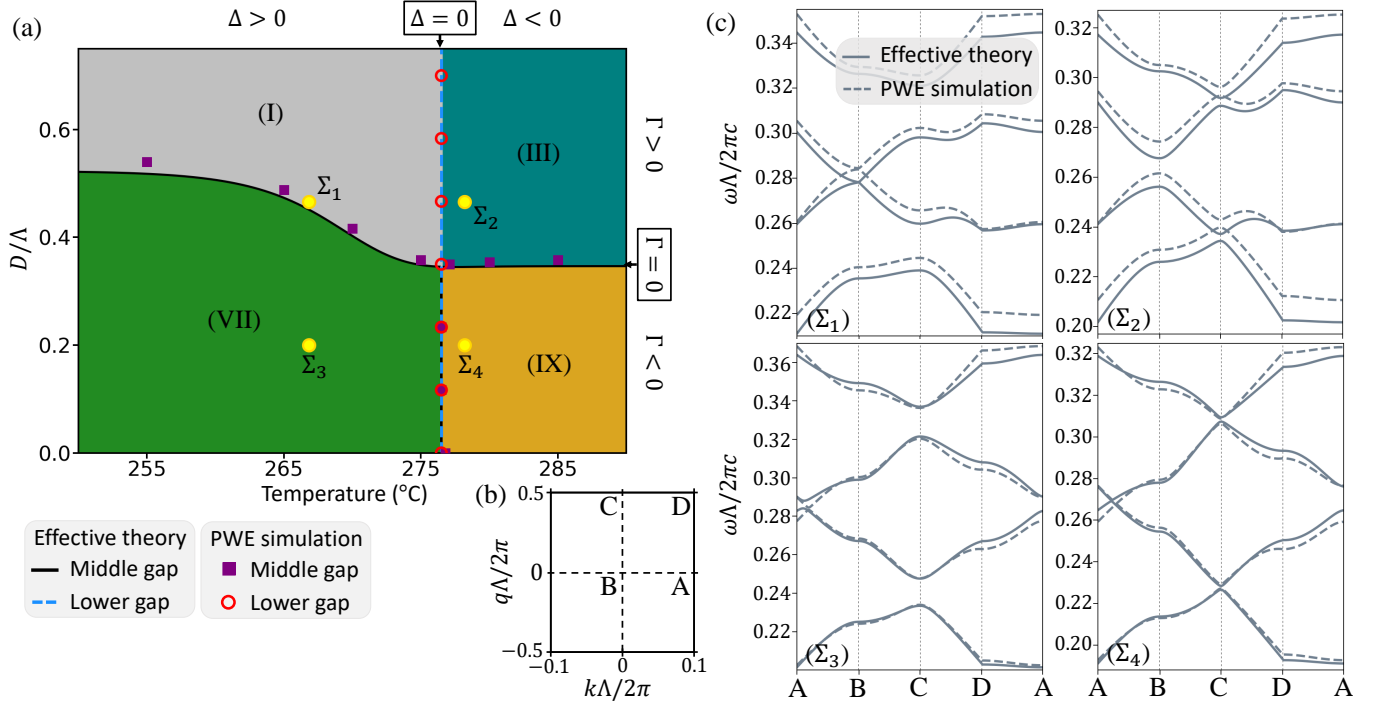


FIG. S2. Comparison between the bulk band structure obtained from PWE simulations and the one calculated by the effective theory. (a) The phase diagram presented in the main text. (b) The contour ABCDA in momentum space that is used to plot the band structures. (c) The four band structures at the four  $\Sigma$ -points in (a).

termed the Hamiltonian and  $\Psi(k) = (C_0 \ C_{-1})^T$ .

The basis functions of this Hamiltonian consists of two plane waves  $\varphi_+ = E_{0y}(z)e^{ik_x x} = E_{0y}(z)e^{i(k+\pi/\Lambda)x}$  and  $\varphi_- = E_{0y}(z)e^{i(k_x-2\pi/\Lambda)x} = E_{0y}(z)e^{i(k-\pi/\Lambda)x}$ . The electric field is hence given by

$$E_y(\mathbf{r}) = E_{0y}(z) \left[ C_0 e^{i(k+\pi/\Lambda)x} + C_{-1} e^{i(k-\pi/\Lambda)x} \right]. \quad (\text{S16})$$

This effective model can be interpreted as depicted in Fig. S1. In a homogeneous slab waveguide with infinitesimal periodic modulation of dielectric constant, two counter-propagating guided modes have group velocity  $\bar{v}$  when their wave numbers are around  $k_x = \pi/\Lambda$  ( $X$  point). In the presence of periodic corrugation, these modes diffract and couple with each other with strength  $U$ . If the grating translates along the  $x$  axis by  $\delta$ , its dielectric function is given by  $\varepsilon'(x) = \varepsilon(x - \delta)$ . While the zeroth Fourier component  $\xi'_0$  remains unchanged, the first component varies as follows

$$\xi'_1 = \int_{-\infty}^{+\infty} dx [\varepsilon'(x) - 1] e^{-i2\pi x/\Lambda} = \int_{-\infty}^{+\infty} dx [\varepsilon(x - \delta) - 1] e^{-i2\pi x/\Lambda} = \int_{-\infty}^{+\infty} dx [\varepsilon(x) - 1] e^{-i2\pi(x+\delta)/\Lambda} = \xi_1 e^{-i2\pi\delta/\Lambda}. \quad (\text{S17})$$

As a result, we arrive at the substitution  $U \rightarrow U e^{-i2\pi\delta/\Lambda}$ .

For the bilayer grating, we can follow a similar procedure to obtain the effective Hamiltonian. However, for simplicity, we treat the problem phenomenologically by assuming that the co-propagating modes in the two layers couple with each other only through the evanescent field. Other interlayer coupling mechanisms are negligible. With the evanescent coupling strength notated  $V$ , we achieve the effective Hamiltonian shown in the main text

$$H(k, \delta) = \begin{pmatrix} \omega_1 + v_1 k & U_1 e^{-i2\pi \frac{\delta}{\Lambda}} & V & 0 \\ U_1 e^{i2\pi \frac{\delta}{\Lambda}} & \omega_1 - v_1 k & 0 & V \\ V & 0 & \omega_2 + v_2 k & U_2 \\ 0 & V & U_2 & \omega_2 - v_2 k \end{pmatrix}, \quad (\text{S18})$$

whose eigenvalues  $\omega(k, q)$  are the frequencies of the four lowest guided modes in the vicinity of the  $X$ -point

$$H(k, \delta) \begin{pmatrix} C_0^u \\ C_{-1}^u \\ C_0^l \\ C_{-1}^l \end{pmatrix} = \omega(k, q) \begin{pmatrix} C_0^u \\ C_{-1}^u \\ C_0^l \\ C_{-1}^l \end{pmatrix}. \quad (\text{S19})$$

Here, the indices  $u$  and  $l$  denote the upper grating and lower grating, respectively. The electric field of these TE modes is given by

$$E_y(\mathbf{r}) = E_{0y}^u(z) \left[ C_0^u e^{i(k+\pi/\Lambda)x} + C_{-1}^u e^{i(k-\pi/\Lambda)x} \right] + E_{0y}^l(z) \left[ C_0^l e^{i(k+\pi/\Lambda)x} + C_{-1}^l e^{i(k-\pi/\Lambda)x} \right]. \quad (\text{S20})$$

For short notations, we write  $E_y(\mathbf{r}) = \sum_{\nu=1}^4 \Psi_\nu \varphi_\nu$  for  $\Psi_\nu \in \{C_0^u, C_{-1}^u, C_0^l, C_{-1}^l\}$  and

$$\varphi_\nu \in \left\{ E_{0y}^u(z) e^{i(k+\pi/\Lambda)x}, E_{0y}^u(z) e^{i(k-\pi/\Lambda)x}, E_{0y}^l(z) e^{i(k+\pi/\Lambda)x}, E_{0y}^l(z) e^{i(k-\pi/\Lambda)x} \right\}.$$

From Figs. S2(c) and S10, we see that the effective model agrees excellently with both PWE and FDTD simulations. We note that in case ( $\Sigma_3$ ) of Fig. S2(c), the two middle bands obtained from PWE simulation has a gap at the AB segment which is small compared to the one given by the effective theory.

## B. Symmetries

- **Time reversal symmetry.** Because the synthetic momentum  $q$  is proportional to a displacement between the two layers, the time reversal action only flip the sign of the real momentum  $k$ , and thus its action in the synthetic momentum space corresponds to  $(k, q) \xrightarrow{T} (-k, q)$ . This action does not represent faithfully the time-reversal symmetry of conventional 2D materials as  $q$  remains invariant under the action. Let  $K$  be the complex conjugation  $KiK^{-1} = -i$ , one can check that

$$H(k, q) = (\mathbb{I} \otimes \sigma_x) K H(-k, q) K (\mathbb{I} \otimes \sigma_x), \quad (\text{S21})$$

thus the time reversal operator is given by

$$T = (\mathbb{I} \otimes \sigma_x) K, \quad (\text{S22})$$

which is expected, since under time reversal transformation, the forward ‘+’ modes and the backward ‘-’ modes are exchanged. This exchange is implemented by the operator  $\mathbb{I} \otimes \sigma_x$ .

- **Spatial inversion.** Here, spatial inversion refers to the  $x$ -reflection. The mirror reflection along  $x$ -axis changes the sign of both the momentum  $k$  and the relative displacement  $\delta$ . Its action corresponds to  $(k, q) \xrightarrow{M_x} (-k, -q)$ . One can check that

$$H(k, q) = (\mathbb{I} \otimes \sigma_x) H(-k, -q) (\mathbb{I} \otimes \sigma_x), \quad (\text{S23})$$

thus the  $x$ -reflection operator is given by

$$M_x = \mathbb{I} \otimes \sigma_x. \quad (\text{S24})$$

Again  $\mathbb{I} \otimes \sigma_x$  implements the switching of ‘ $\varphi_+$ ’ modes and ‘ $\varphi_-$ ’ modes as the consequence of the  $x$ -reflection.

- **Vertical reflection.** If the two layers are identical (i.e.,  $\Delta = 0$ ,  $\omega_1 = \omega_2$ , and  $v_1 = v_2$ ), the system possesses the mirror reflection along the  $z$ -axis. Its action keeps the momentum  $k$  unchanged but switch sign of and the relative displacement  $\delta$ , corresponding to  $(k, q) \xrightarrow{M_z} (k, -q)$ . One can find that

$$H(k, q) = M_z^\dagger H(k, -q) M_z, \quad (\text{S25})$$

with the  $z$ -reflection operator represented by

$$M_z = \sigma_x \otimes \begin{pmatrix} e^{-iq/2} & 0 \\ 0 & e^{iq/2} \end{pmatrix}. \quad (\text{S26})$$

The operator  $M_z$  plays the role of switching layers which is the consequence of  $z$ -reflection.

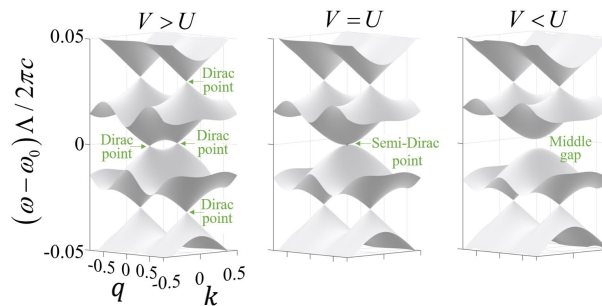


FIG. S3. Band structure of the effective Hamiltonian when the gratings are identical. Three distinct scenarios are presented, corresponding to  $V > U$ ,  $V = U$ , and  $V < U$ .

- **Particle-hole symmetry.** If  $\omega_1 = \omega_2$ , the effective Hamiltonian allows for the particle-hole symmetry

$$-H(k, q) = (\sigma_z \otimes \sigma_y)KH(k, q)K(\sigma_z \otimes \sigma_y), \quad (\text{S27})$$

The particle hole symmetry operator is given by

$$PH = (\sigma_z \otimes \sigma_y)K. \quad (\text{S28})$$

As a consequence of this symmetry, if the eigenstate  $\psi(k, q)$  has frequency  $\omega_{k,q}$ , then the state  $\sigma_z \otimes \sigma_y \psi(k, q)$  is an eigenstate with frequency  $-\omega_{k,q}$ . This symmetry is broken by a difference between  $\omega_1$  and  $\omega_2$ .

### C. Dispersion of homo-bilayer grating

When the two layers are identical ( $\omega_1 = \omega_2 = \omega_0$ ,  $v_1 = v_2 = v$ ,  $\Delta = 0$ ), the four eigenmodes of the effective Hamiltonian (S18) can be analytically derived, and their eigen-frequencies, ordered by increasing values, are given by

$$\omega_1(k, q) = \omega_0 - \sqrt{v^2k^2 + U^2 + V^2 + 2V\sqrt{v^2k^2 + U^2}\cos(q)^2} \quad (\text{S29a})$$

$$\omega_2(k, q) = \omega_0 - \sqrt{v^2k^2 + U^2 + V^2 - 2V\sqrt{v^2k^2 + U^2}\cos(q)^2} \quad (\text{S29b})$$

$$\omega_3(k, q) = \omega_0 + \sqrt{v^2k^2 + U^2 + V^2 - 2V\sqrt{v^2k^2 + U^2}\cos(q)^2} \quad (\text{S29c})$$

$$\omega_4(k, q) = \omega_0 + \sqrt{v^2k^2 + U^2 + V^2 + 2V\sqrt{v^2k^2 + U^2}\cos(q)^2} \quad (\text{S29d})$$

From these expressions, it is straightforward to see that, at  $k = 0$  and  $q = 1/2$ , we have two degeneracies protected by  $M_z$ :  $\omega_1 = \omega_2$  and  $\omega_3 = \omega_4$  for any values of  $U$  and  $V$ . One may demonstrate that these two degeneracies correspond to two Dirac points as shown in cases (II) and (VIII) in the main text. We term them “lower Dirac point” and “upper Dirac point”, respectively.

Moreover, the Eqs. (S29b) and (S29c) suggest that there are three scenarios for these middle branches, as illustrated in Fig. S3 and Fig. 2(a) of the main text:

- **Dominance of intralayer coupling** ( $U > V$ ):  $\omega_2 < \omega_3$  in the whole synthetic momentum space and the bandgap separating them amounts to  $2(U - V)$  [case (II)].
- **Balance between inter- and intralayer couplings** ( $V = U$ ):  $\omega_2 = \omega_3$  at  $k = q = 0$ . At this degeneracy point, the two bands both exhibit semi-Dirac dispersion (quadratic in  $k$  and linear in  $q$ ) but of opposite curvature [case (V)].
- **Dominance of interlayer coupling** ( $V > U$ ):  $\omega_2 = \omega_3$  at  $q = 0$  and  $k = \pm k_D$  with

$$k_D = \frac{\sqrt{V^2 - U^2}}{v}. \quad (\text{S30})$$

These two degeneracies correspond to two Dirac points at zero energy [case (VIII)]. We name them “lateral Dirac points”.

## II. TWO-BAND MODELS

In this section, we present the detailed derivations of the two-band models from the effective (four-band) Hamiltonian (S18) by using the Löwdin partition method. We also comment on the gap opening and closing mechanisms with these models.

We first summarize the procedure to carry out the Löwdin partition for a matrix [70, 71]. This method aims to find an effective matrix from a larger one by perturbation theory. In particular, suppose that we have a Hamiltonian matrix  $H$  that can be written as  $H = H_0 + H'$ , where  $H'$  is a perturbation to  $H_0$ . The unperturbed Hamiltonian  $H_0$  can be diagonalized via a unitary transformation  $\mathcal{U}_s$  so that

$$\mathcal{U}_s^\dagger H_0(k, q) \mathcal{U}_s = \text{diag}(\varepsilon_1, \varepsilon_2, \varepsilon_3, \dots, \varepsilon_N) = \mathcal{H}_0, \quad (\text{S31})$$

where  $\varepsilon_\mu$  are the eigenvalues of  $H_0$  and  $N$  is the dimension of matrix  $H$  and  $H_0$ . The basis states  $\phi_\mu$  of  $\mathcal{H}_0$  are given by  $\phi_\mu = \sum_\nu [\mathcal{U}_s]_{\mu\nu} \varphi_\nu$ . We now try to obtain a two-band Hamiltonian associated with the two eigenvalues  $\varepsilon_\mu$  and  $\varepsilon_\nu$ . First, we apply the unitary transformation  $\mathcal{U}_s$  to the full Hamiltonian  $H$

$$\mathcal{H} = \mathcal{U}_s^\dagger H(k, \delta) \mathcal{U}_s = \mathcal{H}_0 + \underbrace{\mathcal{U}_s^\dagger H' \mathcal{U}_s}_{\mathcal{H}'}. \quad (\text{S32})$$

Applying the Löwdin perturbation method for the two basis states  $\phi_\mu$  and  $\phi_\nu$ , in which the interaction between the two eigenvalues of interest and the others is the perturbation, we obtain the two-band Hamiltonian

$$\tilde{\mathcal{H}} = \tilde{\mathcal{H}}_0 + \tilde{\mathcal{H}}_1 + \tilde{\mathcal{H}}_2 + \dots \quad (\text{S33})$$

with

$$\tilde{\mathcal{H}}_0 = \begin{pmatrix} \varepsilon_\mu & 0 \\ 0 & \varepsilon_\nu \end{pmatrix}, \quad (\text{S34})$$

$$\tilde{\mathcal{H}}_1 = \begin{pmatrix} \mathcal{H}'_{\mu\mu} & \mathcal{H}'_{\mu\nu} \\ \mathcal{H}'_{\nu\mu} & \mathcal{H}'_{\nu\nu} \end{pmatrix}, \quad (\text{S35})$$

$$\tilde{\mathcal{H}}_2 = \begin{pmatrix} h_{\mu\mu} & h_{\mu\nu} \\ h_{\nu\mu} & h_{\nu\nu} \end{pmatrix}, \text{ for } h_{mn} = \frac{1}{2} \sum_l \mathcal{H}'_{ml} \mathcal{H}'_{ln} \left[ \frac{1}{\varepsilon_m - \varepsilon_l} + \frac{1}{\varepsilon_n - \varepsilon_l} \right], \quad (\text{S36})$$

⋮

Next, we apply this method find the effective two-band models for the gaps by considering the bilayer system with  $v_1 \approx v_2$  for simplicity.

### A. Lower and upper gap

As seen previously, the lower and upper Dirac points are pinned at  $(k, q) = (0, 1/2)2\pi/\Lambda$ . We limit the momenta to the vicinity of the Dirac points and define  $p = q - \pi/\Lambda$  with  $p/\Lambda \ll 1$

$$H(k, p) \approx \omega_0 + \begin{pmatrix} d\omega + vk & -(U + \Delta)(1 - ip) & V & 0 \\ -(U + \Delta)(1 + ip) & d\omega - vk & 0 & V \\ V & 0 & -d\omega + vk & U - \Delta \\ 0 & V & U - \Delta & -d\omega - vk \end{pmatrix}. \quad (\text{S37})$$

Here, we have defined  $d\omega = \frac{\omega_1 - \omega_2}{2}$  and  $\omega_0 = \frac{\omega_1 + \omega_2}{2}$ . We use the first-order Löwdin partition method while treating the following matrix as a perturbation

$$H'(k, p) = \begin{pmatrix} vk & i(U + \Delta)p & 0 & 0 \\ -i(U + \Delta)p & -vk & 0 & 0 \\ 0 & 0 & vk & 0 \\ 0 & 0 & 0 & -vk \end{pmatrix}, \quad (\text{S38})$$

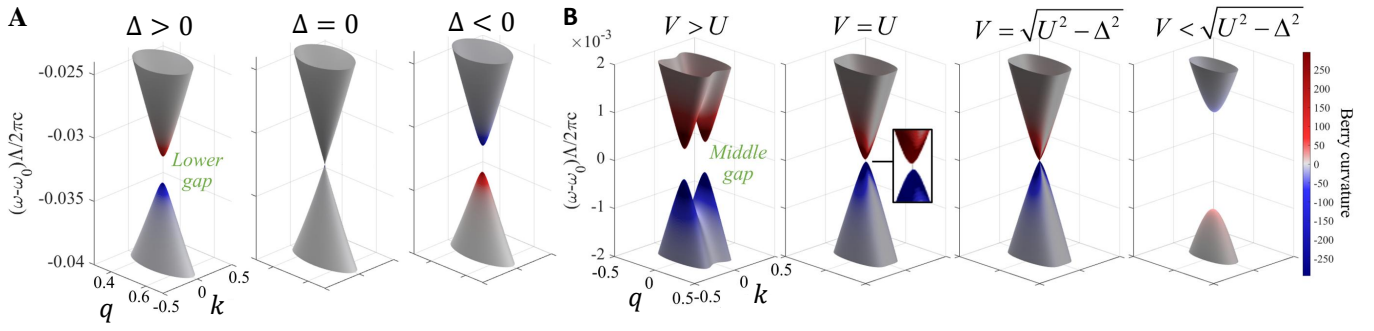


FIG. S4. (a) Dispersion of the lower gap in three cases:  $\Delta = 0.05U$ ,  $\Delta = 0$ , and  $\Delta = -0.05U$ . Here, the interlayer coupling strength is  $V = 1.2U$ . (b) Dispersion of the middle gap in four cases:  $V = 1.05U$ ,  $V = U$ ,  $V = \sqrt{U^2 - \Delta^2}$ , and  $V = 0.95\sqrt{U^2 - \Delta^2}$ . Here, we have chosen  $\Delta = 0.05U$ .

which gives

$$H_{\text{lower}}(k, p) = \omega_0 - \frac{\sqrt{V^2 + (U - d\omega)^2} + \sqrt{V^2 + (U + d\omega)^2}}{2} + \begin{pmatrix} -\Delta - \zeta & \mathcal{F}(k, p) \\ \mathcal{F}^*(k, p) & \Delta + \zeta \end{pmatrix},$$

$$H_{\text{upper}}(k, p) = \omega_0 + \frac{\sqrt{V^2 + (U - d\omega)^2} + \sqrt{V^2 + (U + d\omega)^2}}{2} + \begin{pmatrix} -\Delta + \zeta & \mathcal{F}'(k, p) \\ \mathcal{F}'^*(k, p) & \Delta - \zeta \end{pmatrix},$$

where

$$\zeta = \frac{\sqrt{V^2 + (U - d\omega)^2} - \sqrt{V^2 + (U + d\omega)^2}}{2},$$

$$\mathcal{F}(k, p) = \frac{\mathcal{W}_1 \mathcal{W}_2 - V^2}{\sqrt{V^2 + \mathcal{W}_1^2} \sqrt{V^2 + \mathcal{W}_2^2}} \left[ vk - i(U + \Delta) \frac{\mathcal{W}_1 \mathcal{W}_2}{\mathcal{W}_1 \mathcal{W}_2 - V^2} p \right],$$

$$\mathcal{W}_1 = -d\omega + \sqrt{V^2 + (U - d\omega)^2} + U, \quad \mathcal{W}_2 = d\omega - \sqrt{V^2 + (U + d\omega)^2} + U$$

and

$$\mathcal{F}'(k, p) = -\frac{\mathcal{W}'_1 \mathcal{W}'_2 + V^2}{\sqrt{V^2 + \mathcal{W}'_1{}^2} \sqrt{V^2 + \mathcal{W}'_2{}^2}} \left[ vk - i(U + \Delta) \frac{\mathcal{W}'_1 \mathcal{W}'_2}{\mathcal{W}'_1 \mathcal{W}'_2 + V^2} p \right],$$

$$\mathcal{W}'_1 = d\omega + \sqrt{V^2 + (U - d\omega)^2} - U, \quad \mathcal{W}'_2 = d\omega + \sqrt{V^2 + (U + d\omega)^2} + U.$$

The dispersions of the upper and lower gaps would be the same (just shifted in frequency) if  $\zeta = 0$ , i.e.,  $d\omega = 0$ . This reflects the fact that nonzero  $d\omega$  breaks the particle-hole symmetry. When  $\Delta + \zeta = 0$ , the group velocity along the  $x$  direction of modes at the lower Dirac cone is  $v_F = \frac{|\mathcal{W}_1 \mathcal{W}_2 - V^2|}{\sqrt{V^2 + \mathcal{W}_1^2} \sqrt{V^2 + \mathcal{W}_2^2}} v$ . When  $\Delta + \zeta \neq 0$ , a gap of  $2|\Delta + \zeta|$  is open from the lower (upper) Dirac cone, corresponding to a Dirac mass  $\Delta + \zeta$ . The mechanism is similar for the upper gap.

For  $d\omega = 0$ , the matrices are simplified to

$$H_{\text{lower}}(k, p) = \omega_0 - \sqrt{V^2 + U^2} + \begin{pmatrix} -\Delta & \mathcal{F}_0(k, p) \\ \mathcal{F}_0^*(k, p) & \Delta \end{pmatrix}, \quad (\text{S39})$$

$$H_{\text{upper}}(k, p) = \omega_0 + \sqrt{V^2 + U^2} + \begin{pmatrix} -\Delta & \mathcal{F}_0(k, p) \\ \mathcal{F}_0^*(k, p) & \Delta \end{pmatrix}, \quad (\text{S40})$$

with

$$\mathcal{F}_0(k, p) = -\frac{V}{\sqrt{V^2 + U^2}} \left( vk - i \frac{U + \Delta}{2} p \right). \quad (\text{S41})$$

Both gaps now close when  $\Delta = 0$ . Before and after the gaps close, the Berry curvature has different signs [see Figs. S4(a) and 2], causing a topological phase transition.

**Remarks** – In experimental setups, one cannot change the intralayer coupling  $U$ , the frequency offset  $\omega$ , and the group velocity  $v$  independently. As a result, a small change of  $U$  is accompanied with a change  $d\omega$  of  $\omega$  and  $dv$  of the velocity  $v$ . However, while  $d\omega$  is comparable with  $\Delta$ ,  $dv$  is small and can thus be neglected. This is the case of the heterojunction in the main text but we use the model with  $d\omega = 0$  there to reduce the complexity of the problem.

**Basic waves** – We determine the fundamental modes that serve as a basis for the two-band Hamiltonian. Considering the first-order perturbation, the wave equation is unitarily transformed from  $H(k, \delta)\Psi(k, \delta) = \omega_{k\delta}\Psi(k, \delta)$  to  $\mathcal{H}(k, \delta)\chi(k, \delta) = \omega_{k\delta}\chi(k, \delta)$  with  $\chi(k, \delta) = \mathcal{U}_s^\dagger\Psi(k, \delta)$ . We then limit the eigenvectors to the two new modes, notated as  $\chi_1(k, \delta)$  and  $\chi_2(k, \delta)$  for example, that correspond to the two-band model. From Eq. (S20), we have  $E_y(\mathbf{r}) = \sum_{\nu=1}^4 \Psi_\nu\varphi_\nu = \sum_{\mu, \nu=1}^4 [\mathcal{U}_s]_{\nu\mu}\chi_\mu\varphi_\nu = \sum_{\mu} \chi_\mu \sum_{\nu} [\mathcal{U}_s]_{\nu\mu}\varphi_\nu = \sum_{\mu} \chi_\mu \phi_\mu$  with  $\phi_\mu = \sum_{\nu} [\mathcal{U}_s]_{\nu\mu}\varphi_\nu$ . As a result, the basic waves of the two-band model are given by

$$\phi_1(k, \delta) = \sum_{\nu=1}^4 [\mathcal{U}_s]_{\nu 1} \varphi_\nu(k, \delta) \quad \text{and} \quad \phi_2(k, \delta) = \sum_{\nu=1}^4 [\mathcal{U}_s]_{\nu 2} \varphi_\nu(k, \delta). \quad (\text{S42})$$

We note that the original basic waves  $\varphi_\nu$  are shown below Eq. (S20). For the lower gap, we have

$$[\mathcal{U}_s]_1 = \begin{pmatrix} -\frac{1}{2}\sqrt{1 + \frac{U-d\omega}{\sqrt{V^2+(U-d\omega)^2}}} \\ -\frac{1}{2}\sqrt{1 + \frac{U-d\omega}{\sqrt{V^2+(U-d\omega)^2}}} \\ \frac{V}{2\sqrt{V^2+(U-d\omega)^2}\sqrt{\sqrt{V^2+(U-d\omega)^2}+U-d\omega}} \\ \frac{V}{2\sqrt{V^2+(U-d\omega)^2}\sqrt{\sqrt{V^2+(U-d\omega)^2}+U-d\omega}} \end{pmatrix}, \quad [\mathcal{U}_s]_2 = \begin{pmatrix} \frac{1}{2}\sqrt{1 - \frac{U+d\omega}{\sqrt{V^2+(U+d\omega)^2}}} \\ -\frac{1}{2}\sqrt{1 - \frac{U+d\omega}{\sqrt{V^2+(U+d\omega)^2}}} \\ \frac{V}{2\sqrt{V^2+(U+d\omega)^2}\sqrt{\sqrt{V^2+(U+d\omega)^2}-U-d\omega}} \\ \frac{V}{2\sqrt{V^2+(U+d\omega)^2}\sqrt{\sqrt{V^2+(U+d\omega)^2}-U-d\omega}} \end{pmatrix}. \quad (\text{S43})$$

**Edge modes** – We consider the lower gap when we have a heterojunction of two systems, one with  $\Delta + \zeta > 0$  on the left and one with  $\Delta + \zeta < 0$  on the right. The effective Dirac Hamiltonian of the upper and lower gaps [(S39) and (S40), respectively,] will have opposite masses on the two sides. When  $p = 0$ , the Hamiltonians are 1D Dirac Hamiltonians with opposite masses, and thus we expect a localized zero-energy Jackiw-Rebbi mode at the junction's interface to be observed. In the 2D synthetic momentum space, the localized edge state is chiral along the synthetic dimension  $q$ . As the single Dirac gap changes the sign of its Dirac mass across the junction, the total Berry flux (Chern number) changes by  $\Delta\Phi_{\text{Dirac}} = \pm 1 \times 2\pi$  ( $\Delta C = \pm 1$ ). Consequently, we expect to observe a single chiral edge mode in this configuration at each of upper gap and lower gap [see Figs. 4(b), S12, and S13].

## B. Middle gap

As the physics of the middle gap is more complex than the other ones, we assume here that  $\omega_1 = \omega_2$  to simplify the problem. As we have seen with the upper and lower gap, this approximation does not have great change in the topology of the system.

As the semi-Dirac node is located at  $(k, q) = (0, 0)$ , we consider Hamiltonian (S18) in the vicinity of this point

$$H(k, q) \approx \begin{pmatrix} vk & (U + \Delta)(1 - iq) & V & 0 \\ (U + \Delta)(1 + iq) & -vk & 0 & V \\ V & 0 & vk & U - \Delta \\ 0 & V & U - \Delta & -vk \end{pmatrix}. \quad (\text{S44})$$

Again, we apply Löwdin partition method by treating the following matrix as a perturbation

$$H'(k, q) = \begin{pmatrix} vk & -i(U + \Delta)q & 0 & 0 \\ i(U + \Delta)q & -vk & 0 & 0 \\ 0 & 0 & vk & 0 \\ 0 & 0 & 0 & -vk \end{pmatrix}. \quad (\text{S45})$$

Taking up to the second-order perturbation, we obtain the two-band Hamiltonian

$$H_{\text{middle}}(k, q) = \begin{pmatrix} \mathcal{G}(k, q) & \mathcal{F}(k, q) \\ \mathcal{F}^*(k, q) & -\mathcal{G}(k, q) \end{pmatrix} \quad (\text{S46})$$

with

$$\mathcal{F}(k, q) = -\frac{\Delta}{\sqrt{V^2 + \Delta^2}}vk + i \left( 1 - \frac{\Delta}{\sqrt{V^2 + \Delta^2}} \right) \frac{U + \Delta}{2}q \quad (\text{S47})$$

and

$$\mathcal{G}(k, q) = \Gamma + \frac{(U + \Delta)^2 V^2 q^2 + 3V^2 v^2 k^2 + \frac{V^3}{4U^4} \sqrt{V^2 + \Delta^2} v^4 k^4}{8U(\Delta^2 + V^2)} \approx \Gamma + V^2 \frac{3v^2 k^2 + (U + \Delta)^2 q^2}{8U(V^2 + \Delta^2)}. \quad (\text{S48})$$

We can simplify the Hamiltonian further by using the condition  $\Delta^2 \ll V^2, U^2$  as

$$H_{\text{middle}}(k, q) \approx -\frac{\Delta}{V}vk\sigma_x - \frac{(V - \Delta)(U + \Delta)}{2V}q\sigma_y + \left[ \Gamma + \frac{(U + \Delta)^2}{8U}q^2 + \frac{3v^2 k^2}{8U} \right] \sigma_z \quad (\text{S49})$$

To obtain the form used in the main text, we apply a unitary transformation  $\tilde{U} = \frac{1}{\sqrt{2}}(\sigma_x + \sigma_z)$ , which interchanges  $\sigma_x$  and  $\sigma_z$  while reversing the sign of  $\sigma_y$

$$H_{\text{middle}}(k, q) = \left( \Gamma + \frac{(U + \Delta)^2}{8U}q^2 + \frac{3v^2 k^2}{8U} \right) \sigma_x + \frac{(V - \Delta)(U + \Delta)}{2V}q\sigma_y - \frac{\Delta}{V}vk\sigma_z. \quad (\text{S50})$$

Due to the approximations we have made, the positions of Dirac points when  $\Delta = 0$  are not exactly at  $(\pm k_D, 0)$ . This model can be improved specifically for this case by treating only the  $q$ -dependent part as the perturbation. Nevertheless, as the physics remains unchanged, we only use Hamiltonian (S50) hereafter.

We note that, in Fig. 2 of the main text, the parameters fulfill  $v^2/\Lambda^2 \gg U^2$  and thus  $\frac{(U+\Delta)^2}{8U}q^2 \ll \frac{3v^2 k^2}{8U}$ . As a result, we neglect the parabolic curvature along  $h_y$  direction of the image of the momentum space in the parameter space  $(h_x, h_y, h_z)$  [Fig. 2(b)].

**Basic waves** – Similar to the previous subsection, the components of the eigenvectors of this two-band model are expansion coefficients associated with a new set of basic waves,  $\phi_\mu = \sum_\nu [\mathcal{U}_s]_{\nu\mu} \varphi_\nu$ . We have

$$[\mathcal{U}_s]_1 = \begin{pmatrix} -\frac{1}{2}\sqrt{1 - \frac{\Delta}{\sqrt{V^2 + \Delta^2}}} \\ -\frac{1}{2}\sqrt{1 - \frac{\Delta}{\sqrt{V^2 + \Delta^2}}} \\ \frac{V}{2\sqrt{\sqrt{V^2 + \Delta^2}(\sqrt{V^2 + \Delta^2} - \Delta)}} \\ \frac{V}{2\sqrt{\sqrt{V^2 + \Delta^2}(\sqrt{V^2 + \Delta^2} - \Delta)}} \end{pmatrix}, \quad [\mathcal{U}_s]_2 = \begin{pmatrix} -\frac{1}{2}\sqrt{1 - \frac{\Delta}{\sqrt{V^2 + \Delta^2}}} \\ \frac{1}{2}\sqrt{1 - \frac{\Delta}{\sqrt{V^2 + \Delta^2}}} \\ -\frac{V}{2\sqrt{\sqrt{V^2 + \Delta^2}(\sqrt{V^2 + \Delta^2} - \Delta)}} \\ \frac{V}{2\sqrt{\sqrt{V^2 + \Delta^2}(\sqrt{V^2 + \Delta^2} - \Delta)}} \end{pmatrix}. \quad (\text{S51})$$

### 1. Emergence and merging of Dirac points

When  $\Delta = 0$ , the Hamiltonian (S50) has a similar form with the generic Hamiltonian  $\mathcal{H}_{+-}$  of Ref. [68], which describes the merging of two Dirac points with opposite winding numbers. In our case, when  $U > V$  ( $\Gamma > 0$ ), there is no band-crossing point between the two middle bands. When  $U < V$  ( $\Gamma < 0$ ), these quadratic band splits into two Dirac cones. In the vicinity of the Dirac points  $\vec{k}_{D1} = (2\sqrt{6U(V-U)}/3v, 0)$  and  $\vec{k}_{D2} = (-2\sqrt{6U(V-U)}/3v, 0)$ , the effective Hamiltonian (S50) is approximated as

$$H_{D1}(k, \tilde{k}_1) \approx \sqrt{\frac{3(V-U)}{2U}}v\tilde{k}_1\sigma_x + \frac{U}{2}q\sigma_y, \quad \text{and} \quad H_{D2}(k, \tilde{k}_2) \approx -\sqrt{\frac{3(V-U)}{2U}}v\tilde{k}_2\sigma_x + \frac{U}{2}q\sigma_y \quad (\text{S52})$$

with  $\tilde{k}_1 = k - k_{D1}$  and  $\tilde{k}_2 = k - k_{D2}$ . Comparing the two expressions, we see that the coefficient of  $\tilde{k}_{1/2}$  flips sign. This means that the Dirac cones at  $\vec{k}_{D1}$  and  $\vec{k}_{D2}$  have opposite winding numbers, as expected. When  $U = V$ , the two lateral Dirac cones merge together, forming a semi-Dirac cone.

### 2. Emergence and merging of gapped Dirac valleys

When  $\Delta \neq 0$  and  $V > U$  ( $\Gamma < 0$ ), the middle gap opens and has two valleys related to the two aforementioned Dirac points. As  $V$  decreases, these two valleys move toward each other and merge into a single valley. Once  $\Gamma = 0$ , the middle gap closes at a semi-Dirac point — see Fig. S4(b). The gap opens again when  $\Gamma$  is positive.

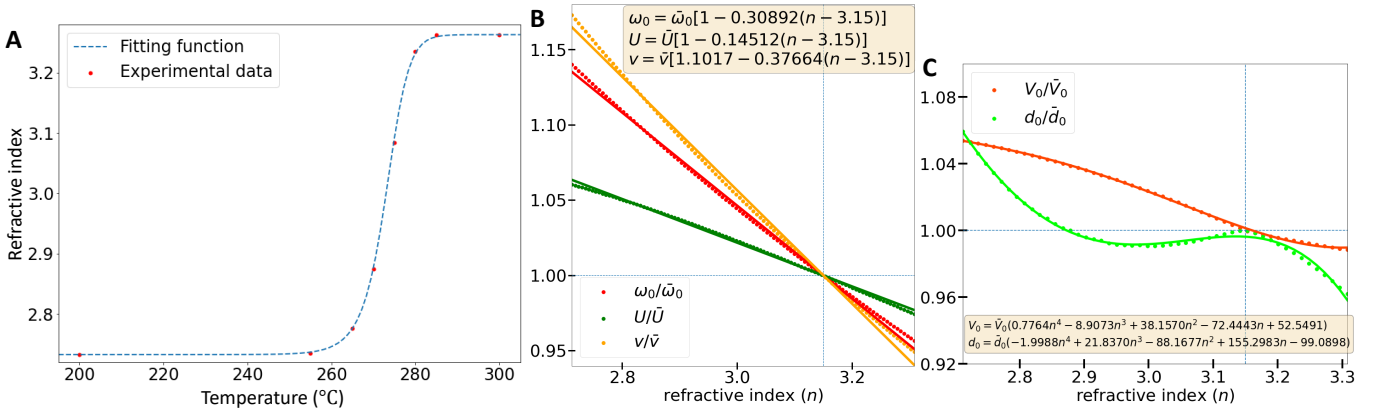


FIG. S5. (a) The dependence of Sb<sub>2</sub>S<sub>3</sub> refractive index on temperature. (b) Variation of model parameters of a single grating ( $L = 0.8\lambda$  and  $H = 0.37\lambda$ ) with respect to the refractive index. (c) Variation of interlayer coupling strength and decay length with respect to the refractive index.

When  $\Gamma < 0$ , in the vicinity of the band edges, the two-band Hamiltonian can be approximated as

$$H_{D1}(k, \tilde{k}_1) \approx \sqrt{\frac{3|\Gamma|}{2U}} v \tilde{k}_1 \sigma_x + \frac{(V - \Delta)(U + \Delta)}{2V} q \sigma_y - \frac{2\Delta\sqrt{6U|\Gamma|}}{3V} \sigma_z, \quad (\text{S53a})$$

$$H_{D2}(k, \tilde{k}_2) \approx -\sqrt{\frac{3|\Gamma|}{2U}} v \tilde{k}_1 \sigma_x + \frac{(V - \Delta)(U + \Delta)}{2V} q \sigma_y + \frac{2\Delta\sqrt{6U|\Gamma|}}{3V} \sigma_z. \quad (\text{S53b})$$

Here, we have used the condition  $\Delta \ll U, V$  so that the term  $\frac{\Delta}{V} v \tilde{k}$  is negligible. We can see that the two models represent two Dirac gaps with opposite masses and opposite winding numbers. Consequently, they have the same Berry curvature and each of them contributes a Chern number  $\pm 1/2$  to the global gap, i.e., the global gap has a Chern number  $\pm 1$ . When the two valleys merge but remain gapped, the total Chern number is unchanged. When the gap closes and opens again for  $\Gamma > 0$ , it becomes trivial.

**Edge modes by connecting  $\Delta < 0$  and  $\Delta > 0$**  – We consider a photonic junction of two systems, one with  $\Delta < 0$  and the other with  $\Delta > 0$ . We have a change of Chern number  $\Delta C = \pm 2$  across the junction. Consequently, we expect to have two chiral edge modes at the interface between the two systems (see Figs. S12 and S14). These chiral modes are degenerate but their degeneracy can be broken by strong disorder at the interface. Nevertheless, their chiral feature remains robust — see Fig. S13.

**Edge modes by connecting  $\Gamma < 0$  and  $\Gamma > 0$**  – The energy gap between the middle bands closes at  $\Gamma = U - \sqrt{V^2 + \Delta^2} = 0$ . Hence, if we consider a photonic junction of two phases with opposite signs of  $\Gamma$  and the same sign of  $\Delta$ , a topological transition is present in this junction. Specifically, the Chern number changes by  $\Delta C = \pm 1$  when  $\Gamma$  switches its sign [see Fig. 2(a)]. We then expect a single chiral edge mode traversing the middle gap to appear at the interface of the junction, which is indeed confirmed by FDTD simulation — see Fig. S15.

### III. TEMPERATURE DEPENDENCE OF ANTIMONY TRISULFIDE

Antimony trisulfide (Sb<sub>2</sub>S<sub>3</sub>) is an ultra-low loss phase-change material. The dependence of its refractive index on temperature for progressive crystallization is presented in the table below, which was provided by the authors of Ref. [77]

Refractive index for wavelength 1500 nm								
Temperature (°C)	200	255	265	270	275	280	285	300
Refractive index	2.732738	2.735401	2.776021	2.87417	3.084485	3.235228	3.26294	3.26295

The continuous change in refractive index arises from gradual partial crystallization. The apparition of nucleation sites of Sb<sub>2</sub>S<sub>3</sub> is reported to have perfectly random and homogeneous distribution [77]. We fit these data with a

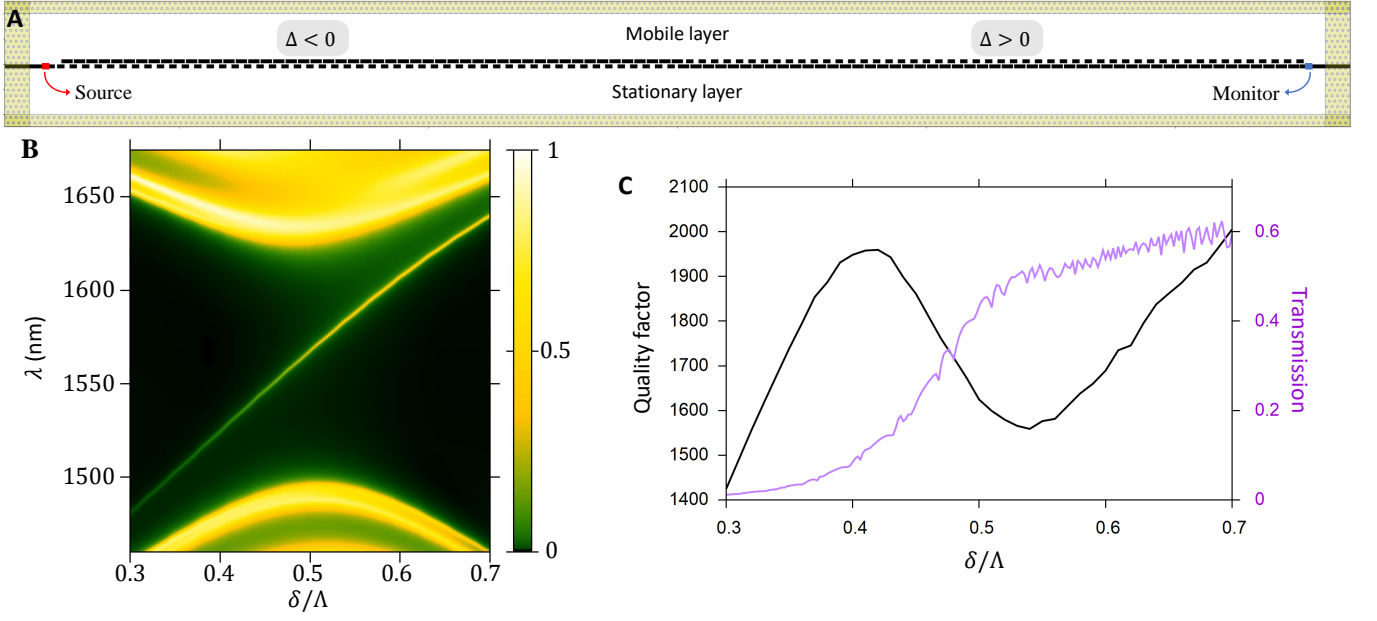


FIG. S6. Photonic junction as a light filter. (a) FDTD computational cell of the heterojunction, which consists of two bilayer gratings with opposite values of  $\Delta$ . The cell is surrounded by phase-matching layers that dissipates the electromagnetic field. (b) The guided transmission spectrum of the system as the upper grating translates gradually. (c) The quality factor and transmission coefficient of the interface mode.

function analogous to the logistic function

$$n_{\text{Sb}_2\text{S}_3} = A + B \left\{ 1 - \frac{1}{1 + 0.5 [e^{\alpha(T-T_0)} + e^{\beta(T-T_0)}]} \right\} \quad (\text{S54})$$

with  $A = 2.732738$ ,  $B = 0.530212$ ,  $\alpha = 0.47062 \text{ K}^{-1}$ ,  $\beta = 0.23360 \text{ K}^{-1}$ , and  $T_0 = 273 \text{ K}$ , as shown in Fig. S5(a).

To obtain the phase diagram in Fig. 7, we retrieve the dependence of model parameters on the refractive index of the  $\text{Sb}_2\text{S}_3$  grating. First, we consider a single  $\text{Sb}_2\text{S}_3$  grating with  $L = 0.8\Lambda$  and  $H = 0.37\Lambda$  and see how the model parameters vary. The simulation data are obtained by PWE with MPB package. We crudely fit the data with linear functions in comparison with parameters ( $\bar{\omega}_0$ ,  $\bar{U}$ , and  $\bar{v}$ ) of an identical grating made of amorphous silicon (aSi), as shown in Fig. S5(b). Then, we examine a bilayer of  $\text{Sb}_2\text{S}_3$  grating and aSi grating with the same geometrical parameters. The interlayer interaction between them is approximated as  $V(D) = V_0 \exp(-D/d_0)$ . The dependence of  $V_0$  and  $d_0$  is fit with polynomial functions – see Fig. S5(c). Here,  $\bar{V}_0$  and  $\bar{d}_0$  correspond to the case when  $\text{Sb}_2\text{S}_3$  refractive index is 3.15, the same as amorphous silicon.

The parameters are

$$\frac{\bar{\omega}_0 \Lambda}{2\pi c^2} = 0.26304, \quad \frac{\bar{U} \Lambda}{2\pi c^2} = 0.02181, \quad \bar{v} = 0.36222c, \quad \frac{\bar{V}_0 \Lambda}{2\pi c^2} = 0.06067, \quad \bar{d}_0 = 0.35599\Lambda.$$

#### IV. GUIDED TRANSMISSION FOR BROADBAND FILTERING

In this section, we demonstrate that a heterojunction of the bilayer grating can be used as a tunable filter.

##### A. Design

The design of the light filter is shown in Fig. S6(a), which is a photonic heterojunction composed of two aligned bilayer gratings on two sides. Each bilayer system consists of two silicon gratings (refractive index 3.5) with identical thickness  $H = 0.3\Lambda$  and different values of width:  $L_1 = 0.9\Lambda$  and  $L_2 = 0.58\Lambda$ . The interlayer separation between the two gratings is  $0.1\Lambda$ . The two sides of the junction share the same structure but the two gratings are swapped, which

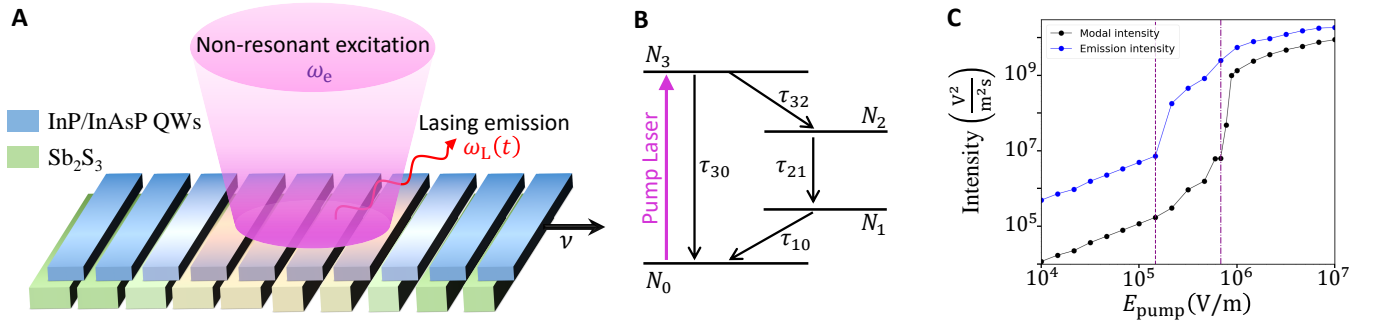


FIG. S7. (a) The heterojunction of bilayer photonic crystal where the upper layer is made of gain material InAsP/InP moves slowly with velocity  $\nu$ . The heterojunction is continuously pumped by a non-resonant spatially Gaussian source of angular frequency  $\omega_e$  and achieves lasing action at  $\omega_L$ . (b) Schematic diagram of the four-level model describing the gain material. (c) Emission and modal intensities with respect to the pump field strength. The dashed line indicates where population inversion starts to take place while the dashed dotted line indicates the lasing threshold.

reverses the sign of  $\Delta$  across the junction. The lower layer is attached stock-still to a source and a monitor, both of which are embedded in a silicon padding block, while the upper layer is mobile and used as a “tunable knob”.

The number of lattice periods per side of the junction is 20. The source emits a pulse with Gaussian shape in frequency, centering at  $0.218c/\Lambda$  and of width  $0.03c/\Lambda$ . The FDTD simulations are carried out using MEEP.

## B. Guided transmission

From the main text, we know that a localized interface mode exists in this junction due to the topological phase transition, and it is chiral along the synthetic dimension  $\delta$ . Importantly, as seen in Fig. 4(d), this mode exponentially decays into the bulk — we can thus excite this mode by putting a source in its decaying tail. The upper layer is translated along the  $x$  direction to tune the frequency of the edge mode by varying  $\delta$ .

The transmission spectrum for various values of  $\delta$  is shown in Fig. S6(b) with lattice period  $\Lambda = 340$  nm. We see that the system in this case can filter a wide range of wavelength, from approximately 1450 nm to 1650 nm[82]. The quality factor of the transmitted signal is shown in Fig. S6(c), which is above 1000, implying the excellent performance of light filtering even for a wide band gap. This quality factor becomes greater when the system size gets larger, i.e., larger  $N$ , as we have seen in Fig. 4(e). However, as the source is further away from the interface, the transmitted signal decreases exponentially. We can optimize the system size to obtain the desirable output as decreasing the size decreases the quality factor but increases the transmission intensity. Additionally, Fig. S6(c) also presents the transmission of the edge mode, which depends strongly on the shift  $\delta$ .

## C. Advantages

Besides being a high-quality filter over a wide range of wavelength, this photonic junction is also a filter robust against disorders and defects. Since the chiral edge mode is topologically protected in the synthetic momentum space, it consistently traverses the spectral gap even in the presence of perturbations — see Fig. S13. Consequently, with the relative displacement  $\delta$  being dynamically adjustable, one can always tune the edge mode to achieve the desirable wavelength.

## V. ADDITIONAL INFORMATION ABOUT THE LASING SIMULATION

In our lasing simulation with Lumerical FDTD - the setup is re-sketched in Fig. S7(a), the gain material is described by a 4-level 2-electron model, which is depicted in Fig. S7(b). In this model, the electron transitions are treated as two coupled dipole oscillators, one corresponds to levels 1 and 2 while the other corresponds to levels 0 and 3. These transitions are governed by the coupled rate equations and the Pauli exclusion principle, and they are solved self-consistently. At  $t = 0$ , the electron populations are  $N_0 = 1$  and  $N_1 = N_2 = N_3 = 0$ . Other parameters are given in the Materials and Methods.

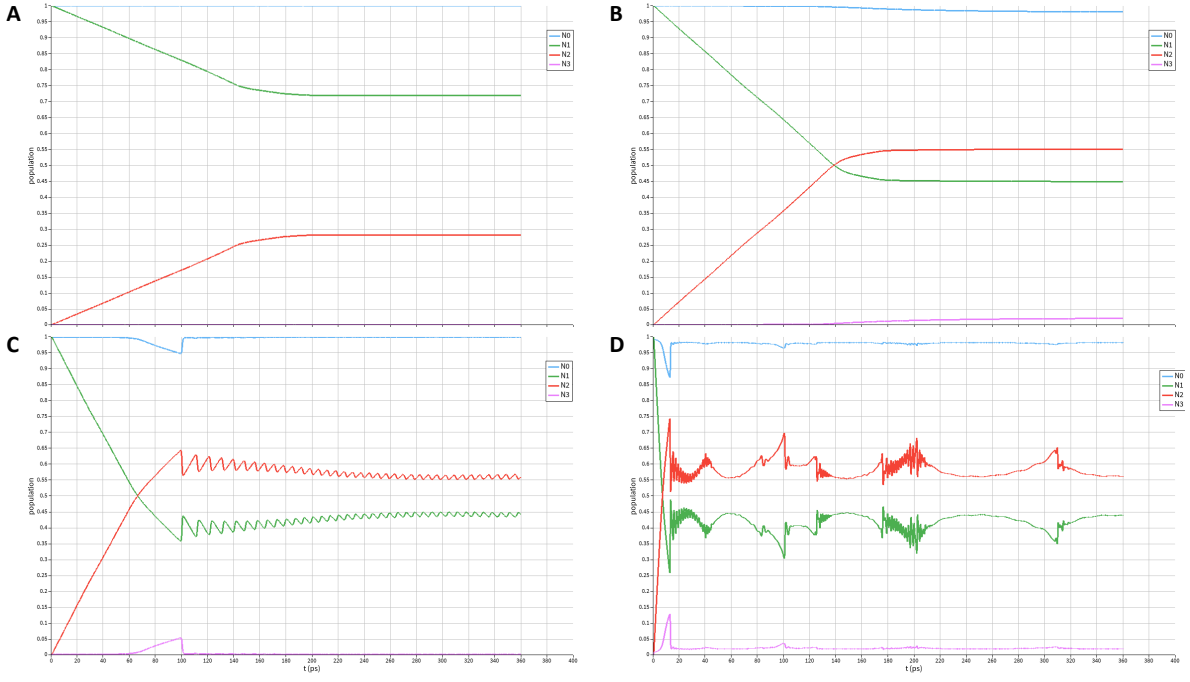


FIG. S8. Electron population density probability of the four levels at different pump field strengths: (a)  $E_{\text{pump}} = 10^5$  V/m, (b)  $E_{\text{pump}} = 146780$  V/m, (c)  $E_{\text{pump}} = 215440$  V/m, (d)  $E_{\text{pump}} = 316230$  V/m.

when examining the lasing action with respect to the field strength of the pump at  $\delta = 0.5\Lambda$ , there are two ways to present the emission signal. The first one is to compute the lasing modal intensity, which is shown in the main text. Here, we focus solely on the intensity of light at the lasing wavelength. The second way is to compute the emission intensity, which is also defined by  $\frac{1}{2\pi} \int d\omega |E|^2$  but with the integration taken over the frequency range  $\omega$  encompassing all the emission peaks. Both of these quantities are shown in Fig. S7(c) against the pump field strength. On the one hand, we see that the modal intensity illustrates well the lasing threshold  $E_{\text{thres}} \approx 7 \times 10^5$  V/m where the lasing peak starts to appear. On the other hand, the emission intensity depicts nicely where the population inversion (between level 1 and 2) starts to take place, which is  $1.5 \times 10^5$  V/m. The electron populations at some values of field strengths around this transition are shown in Fig. S8.

Here, the population inversion occurs at pump field strengths smaller than the lasing threshold due to the amplified spontaneous emission. This is expected since due to large volume of the gain material, i.e., the whole upper layer.

## VI. EDGE STATE FROM EFFECTIVE MODEL

In Figure 5D of the main text, we use the effective model to compute the chiral edge mode within the synthetic space, which serves as a guide for the simulation results. The method for this calculation is detailed in the Supplemental Material of Ref. [83].

## VII. SUPPLEMENTAL FIGURES

Here we present additional data for several cases of bilayer silicon gratings. The geometrical parameters of interest are  $\kappa = L/\Lambda = 0.8$  and  $\eta = H/\Lambda = 0.37$ . Other cases are achieved by slightly modifying these parameters. In the figures below, we also change the notation  $(k, q)$  to  $(q_x, q_y)$ .

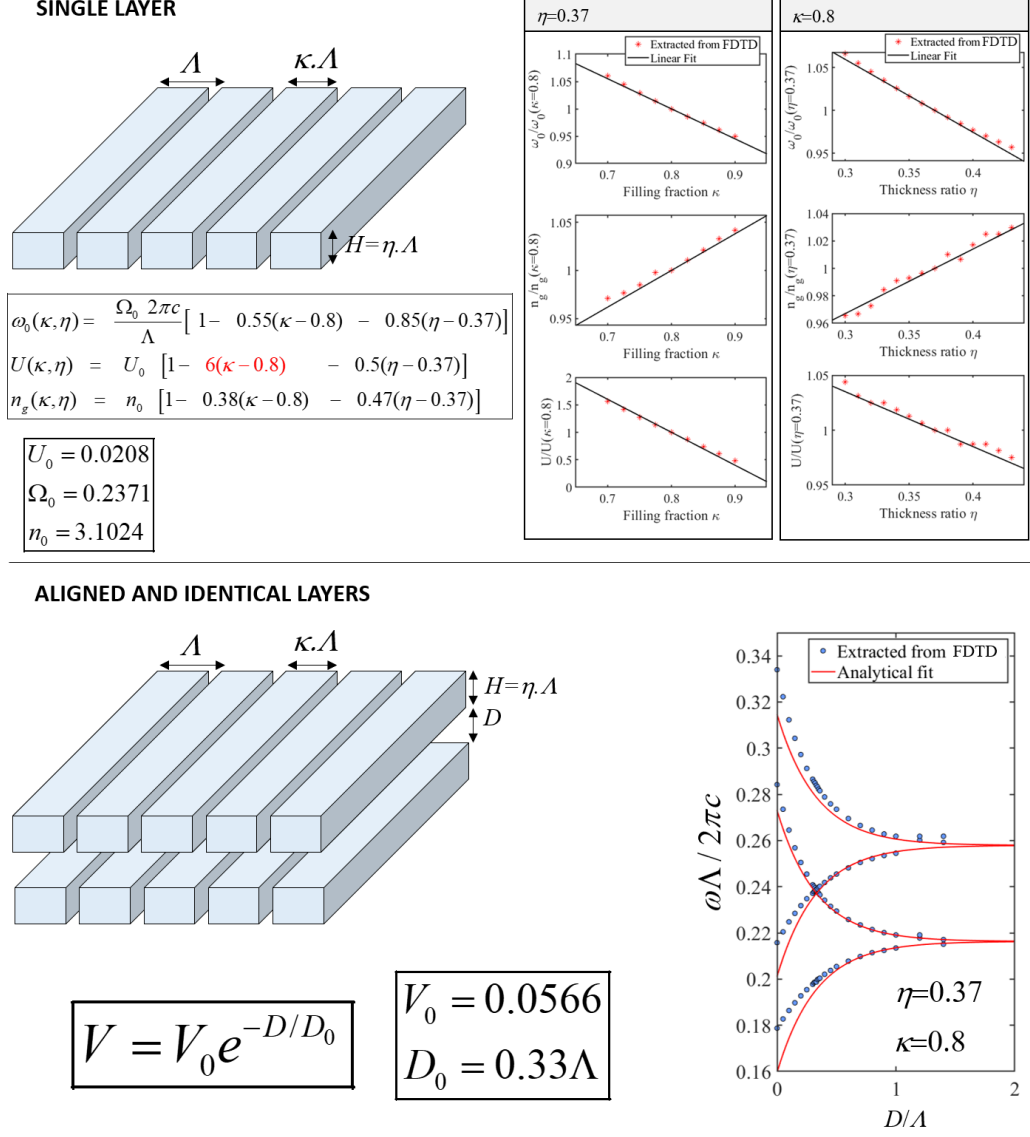


FIG. S9. Parameter retrievals for the effective Hamiltonian from FDTD simulations. Upper Panels: the simulations for a single layer grating are used to obtain the dependence of  $\omega_0$ ,  $U$  and  $n_g$  as functions of the filling fraction  $\kappa$  and thickness ratio  $\eta$ . These parameters are extracted by fitting the two band dispersion with the Hamiltonian (S15). Lower Panels: the simulations for a bilayer of aligned and identical gratings at  $q_x = 0$  are used to obtain the dependence of  $V$  as functions of the distance  $D$  separating the two layers. The exponential decay law of  $V$  is obtained by fitting the four band edges  $\omega_0 + U + V$ ,  $\omega_0 + U - V$ ,  $\omega_0 - U + V$ , and  $\omega_0 - U - V$  at varying distance  $D$ . Here, the values of  $U$  and  $\omega_0$  are already known from the retrievals from the single layer simulations.

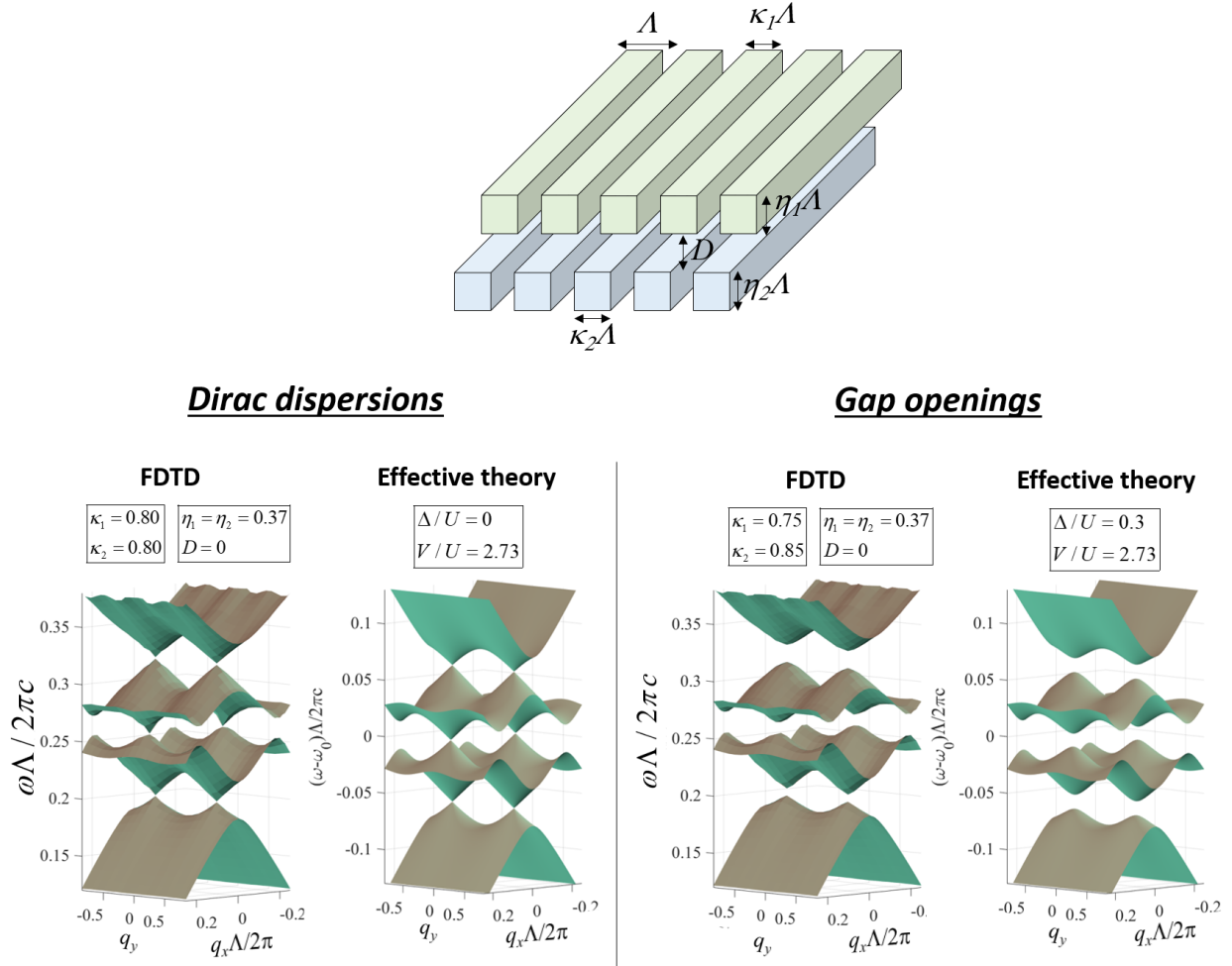


FIG. S10. Comparison between the bulk band structure obtained from FDTD simulations and the one calculated by the effective theory using the retrieved parameters shown in Fig. S9. Here, the simulated band structures are only shown in the vicinity of  $q_x = 0$  (i.e.,  $X$  point of the 1D Brillouin zone) since the effective theory is only valid in this region.

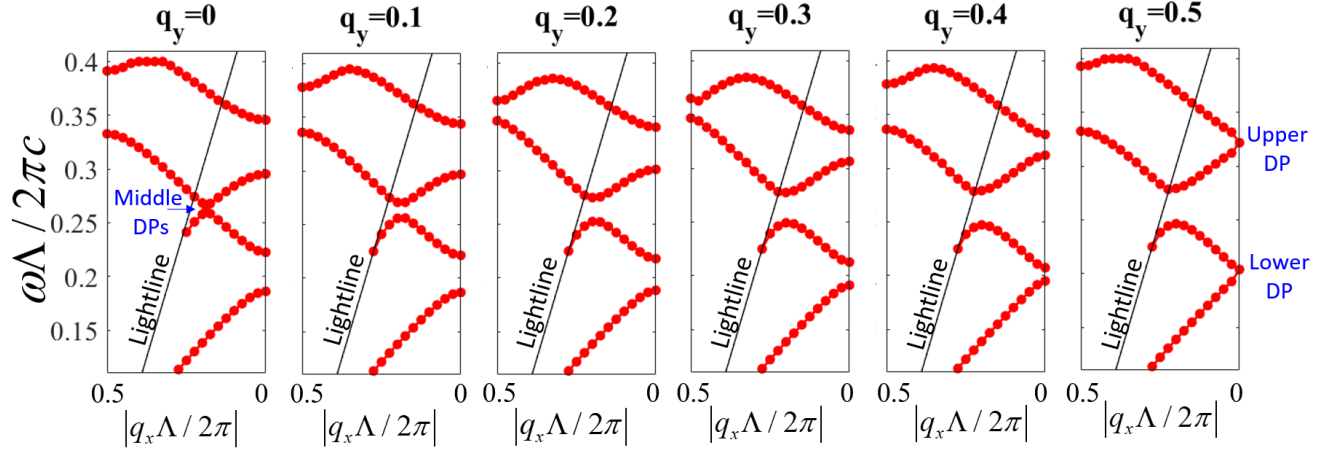


FIG. S11. Full band structure of the bulk given by FDTD simulations for the case  $\kappa_1 = \kappa_2 = 0.8$ ,  $\eta_1 = \eta_2 = 0.37$  and  $D = 0$ . It shows that while the lower Dirac point and the middle Dirac points are well spectrally isolated, it is not the case for the upper Dirac point since there are bulk bands at the same energy at high wave vector.

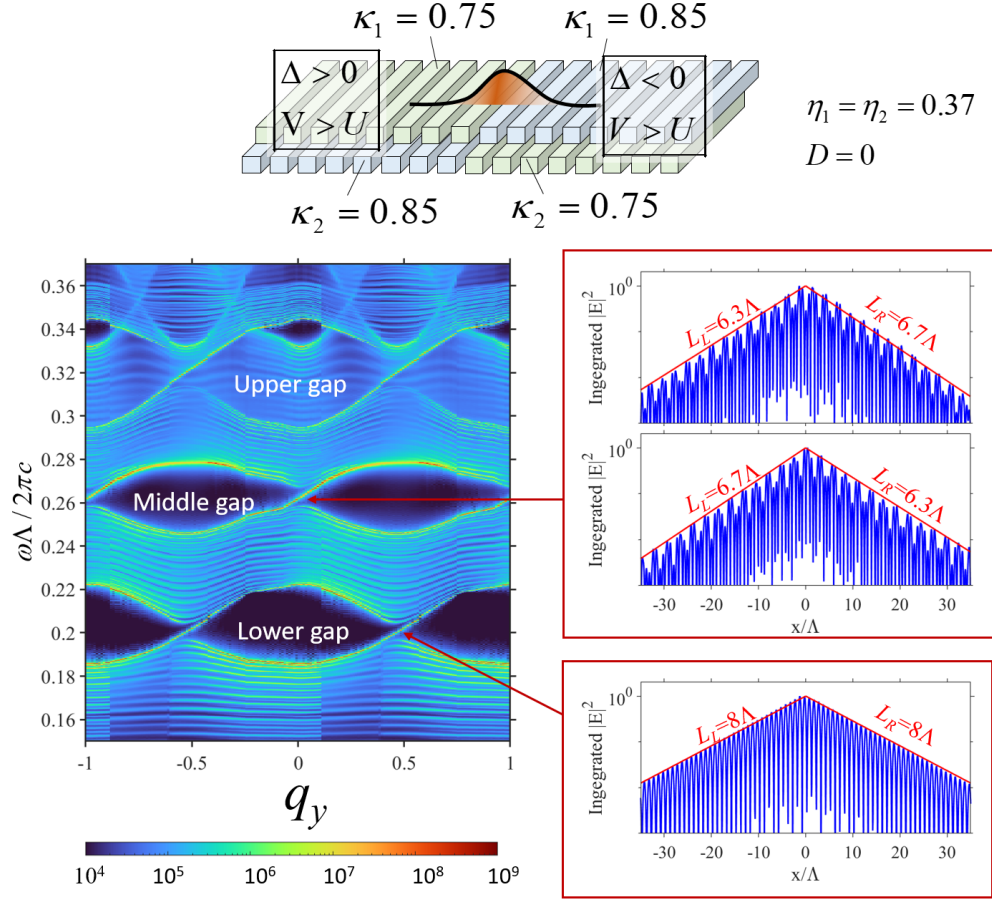


FIG. S12. Topological edge states from the heterostructure composed of two topological phases having opposite  $\Delta$  value. Here, the spectra along  $q_y$ , numerically calculated by FDTD, is shown within two periods of  $q_y$  and with the full energy scale of the four bulk bands. There are bulk bands that are not described by the effective theory cross the upper gap. Thus only the Middle gap and Lower gap are considered for edgestates.

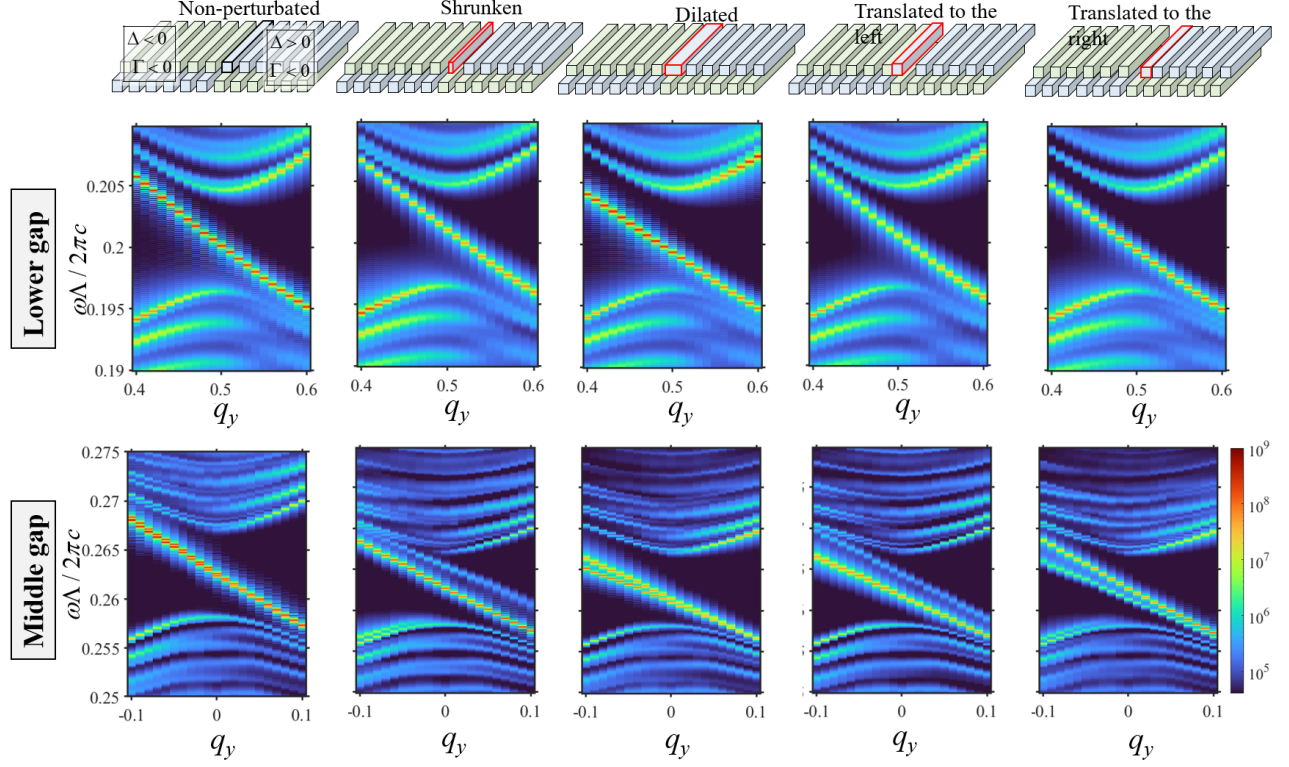


FIG. S13. The robustness of the chiral edge states in Fig. S12 against defects at the interface. Here, the interface is strongly perturbed by modifying either the size or the position of the first rod in the upper-right grating. These results show that: i) the chirality is topologically protected against perturbations, and ii) the degeneracy lifting of the two edge states in the middle gap depends strongly on the interface, i.e., the boundary conditions.

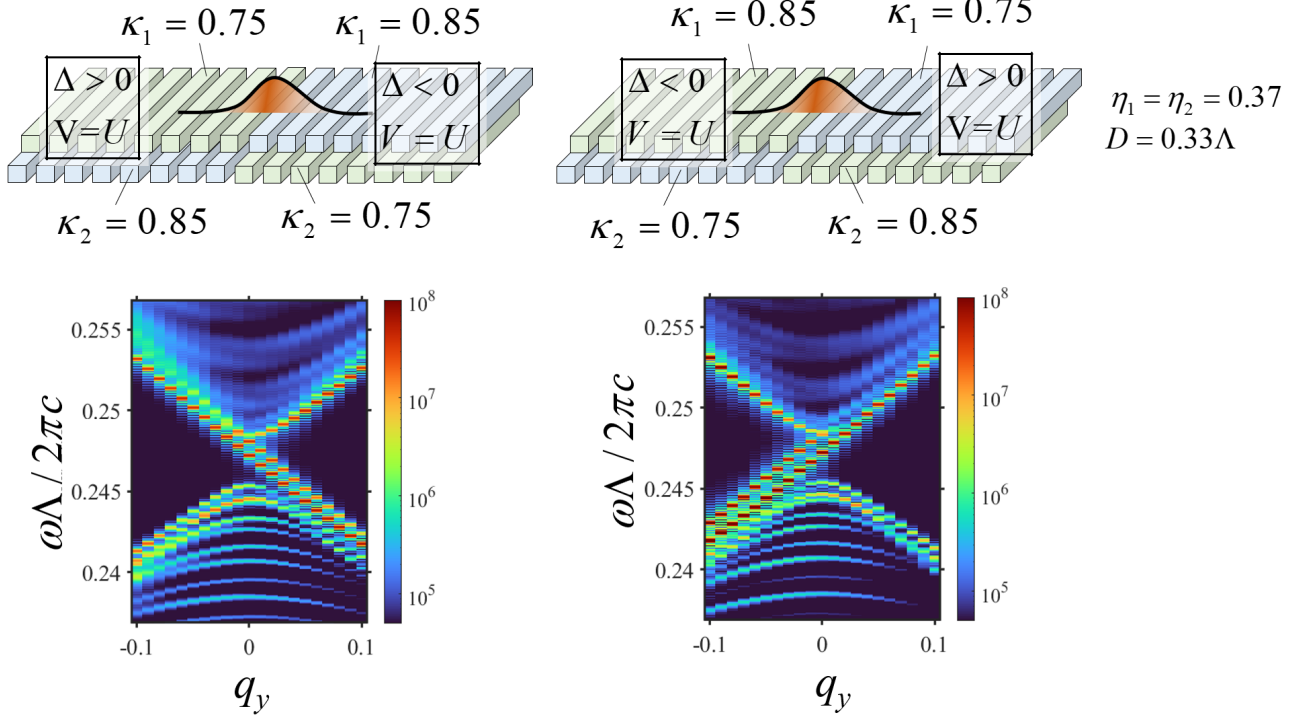


FIG. S14. Topological edge states traversing the middle gap in two heterojunctions composed of two topological phases having opposite  $\Delta$  value. Here, the design corresponds to the special case  $V = U$  at which we have the merging of the two mini-middle gaps (see Fig. S4b for the bulk band structure). When  $U < \sqrt{V^2 + \Delta^2}$ , topologically, the change of the total Berry flux when switching the sign of  $\Delta$  equals to the change when switching the sign of the Dirac masses of the two lateral Dirac cones. Therefore the difference of total the Berry flux between the left and the right sides is  $4\pi$ , which also implies the difference of the Chern number  $\Delta\mathcal{C} \pm 2$  between the left and the right sides. Consequently, we expect two edge modes in this configuration.

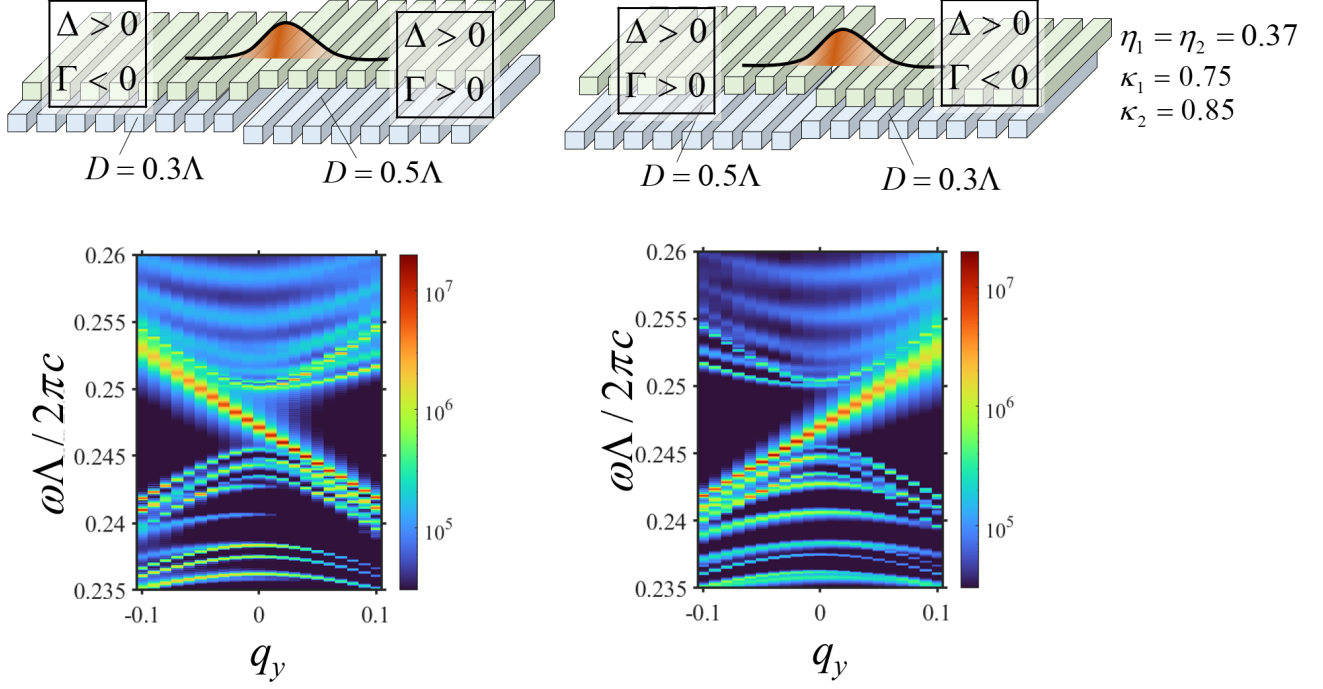


FIG. S15. Topological edge states traversing the middle gap in two heterojunctions composed of two topological phases having opposite  $\Gamma$  value. From the effective Hamiltonian of the middle bands (S49), we see that the two bands are described by a Dirac Hamiltonian of mass  $\Gamma$ . When we switch the sign of  $\Gamma$ , the change of the total Berry flux is  $\pm 2\pi$ , which means that the difference of the Chern number is  $\Delta C \pm 1$  between the left and the right sides. Consequently, there should be only one edge mode.